Weathering of Viamão granodiorite, South Brazil: Part 1 – Clay minerals formation and increase in total porosity

M. Bonnet, L. Caner, M. Siitari-Kauppi, A. Mazurier, A.S. Mexias, N. Dani, Paul Sardini

Weathering of Viamão granodiorite, south Brazil:

Part 1 – clay mineral formation and increase in total porosity

M. Bonnet[1], L. Caner[1], M. Siitari-Kauppi[2], A. Mazurier, A. S. Mexias[3], N. Dani[3], and P. Sardini[1]

[1]University of Poitiers, UMR CNRS 7285 IC2MP, HydrASA, rue Albert Turpain, Bâtiment B8, 86022 Poitiers, France, [2]University of Helsinki, Department of Chemistry, P.O. Box 55, 00014 University of Helsinki, Finland, [3]Instituto de Geociências, Universidade Federal do Rio Grande do Sul – UFRGS, 91501-970, Porto Alegre, RS, Brazil.

ABSTRACT

Weathering transforms fresh un-weathered rock into saprolite and soils, porous materials that may hold available water for plants and nutrients. The conjoint characterization of mineral weathering and development of porosity is helpful in understanding rock weathering and the development of soil.

The objective of this study was to investigate mineralogical transformations and the increase in total porosity during granodiorite weathering in South Brazil by combining petrographical observations, mineralogical analyses, and porosity measurements. The studied granodiorite profile presented a saprock of ~2m thickness with spheroidal weathering, a ~ 15 m thick saprolite of and soil of ~ 2 m thickness. The intensity of weathering was estimated using chemical indices (CIA and WIS) and by the production of fines particles of silt and clay sizes. As weathering increased from saprock to saprolite and soils total porosity increased from 1.73 % in the un-weathered rock, between 3.57 and 10.5 % in the saprock and 11.02 % in the

saprolite. The chemical losses were limited in saprock and saprolite (CIA = 68, Δ4Si = 29.31 %) and increased in the topsoil (CIA = 85.73, Δ4Si = 56.83 %), indicating a moderate weathering intensity. Petrographic observations by optical microscope and SEM, chemical composition using SEM-EDS and X-ray diffraction results showed principal mineral weathering reactions were the transformations of biotite into vermiculite (with biotite/vermiculite mixed layers as intermediate weathering stages) and weathering of plagioclases and potassic felspars into kaolinite. The multi-mineral composition of the saprolite indicated a progressive transformation of primary minerals with increasing weathering intensity. The results show that the opening of the porosity is likely to control the development of the weathering and should deserve more detailed characterisation.

KEYWORDS

Weathering, porosity, clay minerals, granodiorite, biotite, feldspars

1. INTRODUCTION

Weathering is the transformation of rocks at the surface of the earth by chemical and physical processes that play a key role in the nutrient and water cycles in soils and ecosystems. The nutrient elements that are inaccessible to living organisms in primary minerals are released in an available form in the thin layer of soil at the surface critical zone (Sternberg et al., 1996; Wilson, 2004; Rossi and Graham, 2010; Graham et al., 2010; Brantley, 2010; Navarre-Sitchler et al., 2015). During weathering and soil formation, primary minerals are progressively replaced by newly formed secondary minerals such as clays minerals and iron and aluminium oxy-hydroxides, the dominant inorganic constituents of soils. The slightly acidic (dissolution of CO_2 and dissolved organic matter) and oxidizing meteoric fluids

percolating in the soils, the critical zone, and into the rock through cracks and inter-grain joints causes the weathering of minerals by processes operating at their surface (Hochella and Banfield, 1995; Lee et al., 1998; Eggleton and Buseck, 1980, Meunier et al., 2007, Brantley et al., 2014). The weathering mechanisms are driven by the water/rock interactions at a small scale (few nm to µm) at the interface between un-weathered rock and saprock, i.e., at the weathering fronts. The formation of the secondary minerals (clays and oxy-hydroxides) is controlled by the concentration of chemical elements of the fluids in the weathering microsystems (Meunier et al., 2007).

Weathering can be treated as a diffusive process as it depends on the diffusion of chemical species in and out of the weathering systems (Fletcher et al., 2006; Hoke and Turcotte, 2002, 2004; Navarre-Sitchler et al., 2013). The early stages of rock weathering are dominated by water flow along joint planes. Mass transport and fluid–rock interactions are controlled by the fraction of the total pore space that forms an interconnected micro-fracture net (Siitari-Kauppi et al., 1997; Navarre-Sitchler et al., 2013, 2015; Bazilevskaya et al. 2013, 2015; Buss et al., 2017). The weathering causes the dissolution of unstable silicate minerals and thus the formation of pores and also micro-fractures in the rock, for example, the expansion of biotites strongly participates in the opening of cracks and the increase of the total porosity of the weathered rock (Eggleton and Buseck, 1980; Hochella and Banfield, 1995; Lee and Parsons, 1995; Lee et al., 1998; and Velde and Meunier, 2008; Rossi and Graham, 2010; Graham et al., 2010, Sardini et al., 2006). Weathering thus induces chemical (i.e., losses or gains of elements) and physical changes (i.e., strain, hydraulic conductivity) of the rock. In the initial stage of weathering, primary minerals and microcracks predominate in coherent un-weathered rock and chemical processes mainly produces secondary minerals (illite, vermiculite, smectite, and mixed layers minerals). At this stage (saprock or saprolite), the rock suffering weathering is composed in one hand of weathered zones with enhanced connected pore

network and, the second of un-weathered mineral aggregates with low porosity (intergranular joints, cleavages, microcracks). The clay mineral assemblages are complex and multi-mineral resulting from water/rock interactions in separated several microsystems (Meunier et al., 2007, Velde and Meunier, 2008). The total porosity and the amount in fine fraction (clays and silts) increases and as a result the bulk density decreases (Jones and Graham, 1993; Graham et al., 1997; Frazier and Graham, 2000). With the increase in weathering intensity 1:1 kaolinite clay mineral is formed, and its abundance progressively overcome that of other clay minerals, to become dominant with iron aluminium oxy-hydroxides in highly weathered tropical soils (Meunier et al., 2007; 2013, Wilson, 2004).

The weathering of crystalline rocks, which is the focus of this study, is controlled by the chemical and mineralogical compositions of the rocks. The factors that play a key role are the contents in SiO_2, MgO, Fe_2O_3, K_2O, and the presence in highly weatherable minerals such as ferro-magnesian (e.g., biotite), moderately weatherable minerals such as plagioclases and minerals more resistant to weathering like K-feldspars, muscovite and finally quartz (Velde and Meunier, 2008; Heckman and Rasmussen, 2011; Bazilevskaya et al. 2013, 2015; Buss et al., 2017; Navarre-Sitchler et al., 2015).

Strictly speaking, the weathering of crystalline rocks also depends on opportunities for pore networks to develop (Twidale, 1982; Turner et al., 2003; Navarre-Sitchler et al., 2015). Connected porosity refers to microscopic cracks/fractures and physical defects within and between minerals (which defines rock permeability) but also macroscopic joint systems (Twidale, 1982). For example, Gunnell and Louchet (2000) have demonstrated in south India and Sri Lanka that the low weathering rates of charnockites were not controlled by their lithology but by the fact that these rocks are very poorly fractured at the scale of the massifs and very poorly porous. As a result, few paths are possible for water infiltration and consequently the alteration is weaker than that of the gneisses (Navarre-Sitchler et al., 2015).

Rock weathering that implies the dissolution of primary minerals and precipitation/crystallisation of secondary ones changes the bulk chemistry of the rock but also its physical properties such as total porosity, tortuosity of pore network, aperture of the pores and related permeability, water flow, diffusivity, and mechanical strength (Navarre-Sitchler et al. 2009). The porosity created by weathering increases the water holding capacity and the water accessibility to living organisms; and water flow in the critical zone (Wilson 2004; Meunier, et al., 2007; Navarre-Sitchler, et al., 2009; 2015, Rossi and Graham, 2010; Graham et al., 2010).

To understand weathering processes, it is thus necessary to study mineral transformations and textural changes of the rock (total porosity, pore space/size distribution, hydraulic conductivity). They are both the key parameters controlling weathering and the kinetics of transformations.

Here we present the effect of weathering on the conjoint modification of mineral and porosity in a thick soil profile of south Brazil developed on granodiorite basement. Because the result of rock weathering involves the alteration of primary minerals in quite complex mineral phases such as clays, it was necessary to carefully analyse the phyllosilicates.

The conjoint evolution of porosity with weathering intensity will be examined in bulk in this paper. The coupled modifications of porosity and mineralogy are presented in the companion paper (Bonnet et al., submitted).

2. MATERIALS AND METHODS

2.1 Location, geological setting, and environmental conditions

125 The weathering profile studied is located in a granodorite quarry in the municipality of
126 Viamão (30° 09' 66'' S; 51° 03' 15'' W), 25 km east of Porto Alegre in the State of Rio
127 Grande do Sul (RS), southern Brazil (Figure 1a). The Viamão Granodiorite shows a soft-
128 wavy reliefs, without much elongation of valleys or uplifted areas. In the eastern and northern
129 extremity of the studied area, the presence of a NE and SW ruptile tectonics, associated with
130 normal faults, promotes the appearance of grabens and horsts. To the east, partially eroded
131 fault scarps appear, which limit Quaternary terraces of the Coastal Province with
132 undifferentiated Cenozoic sediments, transitioning to a flat relief with ridges marked by small
133 granitic hills. The area is covered by degraded Atlantic forests, crop areas and granodiorite
134 quarries. The regolith profile is underlain by the Viamão-Granodiorite unit (Figure 1b) dated
135 of Neoprotorozoic age (~600 Ma, Philipp et al., 1998, 2002) and, described as intrusive,
136 potassium-rich, calco-alkaline granodiorite and monzogranites.
137 The region has a subtropical climate with a mean annual rainfall of 1550 mm / year that is
138 evenly distributed over the year, and a mean annual temperature of 18 to 20°C.
139

140 **2.2 Weathering profile description and sampling**

141

142 The weathering profile of an approximate thickness of 20 m is divided into four parts: the un-
143 weathered rock, the saprock, the saprolite and the soil (Supplementary Figure 1). The un-
144 weathered rock appears as large boulders of dark grey color in the bottom of the profile
145 underlain by the granodiorite outcrops. The granodiorite contains large phenocrysts of
146 orthoclase (2-3 cm) and equigranular crystals (0.5-1 cm) of quartz, plagioclases, and biotite.
147 In some places of the outcrops, shearing figures are observed with alternated quartz-feldspars
148 ribbons indicating local mylonitization. Philipp et al. (2002) also described monzogranites
149 with oligoclase and andesine.

150 The saprock, of an average thickness of two meters, is formed during the first stage of the
151 weathering process. The rock conserves its initial structure but is mechanically less resistant.
152 Intercrystalline cracks are formed making the rock friable. The phenocrysts of potassic
153 feldspars, plagioclases, quartz, and biotite are still visible to the naked eye and the latter one
154 presents orange-brown halos indicating alteration. The weathering increases with the distance
155 from the boulder as shown by a change in colour and lower mechanical resistance.
156 In the saprock the structure of the un-weathered rock is preserved and maintained even though
157 the rock is partially weathered, and its mechanical resistance is reduced (breakable by hand).
158 Saprock results from the partial dissolution of the primary minerals of the rock and the
159 presence of cracks formed by the circulation of meteoric water within the pre-existing cracks
160 of the un-weathered rock.
161 In the saprolite (or gruss) the structure of the un-weathered rock is no longer preserved, it is
162 totally disintegrated and friable (crumbled by hand) due to the weathering of biotite and
163 feldspars that are no more joined. It is the thickest part of this profile that extends over about
164 15 metres in height. The bottom of the saprolite and the saprock contain un-weathered
165 corestones of several dm to m in diameter surrounded by onionskin like structures (spheroidal
166 weathering).
167 The soil, on the top of the weathering profile forms a 2 m thick and clay-rich layer containing
168 a low proportion of sand. Its reddish-ochre colour is due to the presence of iron oxy-
169 hydroxides. Quartz and some mica flakes are observed with the naked eye.
170 Sampling was conducted so that each part making up the weathering profile was represented:
171 un-weathered rock GRV01; saprock with increasing weathering GRV02, GRV03, GRV04,
172 VIA05, VIA04 and GRV05; saprolite GRV06, GRV07, VIA01, VIA03, VIA02, GRV08,
173 GRV09 et GRV10; soil GRV11. The sampling was done continuously in the different zone
174 after description to identify changes in colour, texture, or mechanical resistance. The different

175 samples were not mixed to evidence the gradual changes in chemical composition and
176 mineralogy.
177 Undeformed samples were collected for petrographic and porosity analyses in the different
178 levels except the top of the saprolite (too friable) and the soil. In the saprock the undeformed
179 samples correspond to different weathered rindlets from onionskin like structures surrounding
180 the un-weathered corestone boulders. In the saprolite the samples were collected at the same
181 position than bulk samples but in metal boxes to avoid fractures during transport.
182
183 **2.3 Chemical and physical investigation methods**
184
185 *2.3.1 Chemical analyses*
186
187 The chemical compositions for major elements were determined for all samples by
188 inductively coupled plasma atomic optical emission spectrometry (ICP-OES) after fusion with
189 lithium metaborate $LiBO_2$ at the CNRS Service d'Analyse des Roches et des Minéraux
190 (SARM) (Carignan et al., 2001; http://www.crpg.cnrs-nancy.fr/SARM/index.html). Before
191 the fusion the samples (~10g) were ground with a McCrone Micronising Mill (< 5 µm) to
192 ensure homogeneity of the analysed sample.
193 Two weathering indices were calculated to quantify the degree of weathering based on the
194 weight percent oxides values obtained from total chemical analyses. The Chemical Index of
195 Alteration (CIA) was calculated using element molar proportions (Nesbitt and Young, 1982)
196 with the following equation:
197
$$CIA = \frac{Al_2O_3}{Al_2O_3 + Na_2O + CaO^* + K_2O} \times 100$$

198 CaO* corresponds to the CaO associated to the silicates by removing the contribution of
199 apatite (CaO* = CaO – ((10/3) × P_2O_5)). The CIA quantifies the weathering intensity by

200 estimating the losses in Ca^{2+}, Na^{+} and K^{+} and the relative accumulation of residual
201 aluminium. Intense weathering results in large values of CIA (70-100%). The Weathering
202 Intensity Scale (WIS – Meunier et al., 2013) was calculated, after conversion of oxides wt% into molar cationic values, using the Δ4Si (difference between the compositions in silica of
204 un-weathered and weathered samples):

205 $$\Delta 4Si = \frac{4Si_{weathered\ sample} - 4Si_{un-weathered\ rock}}{100 - 4Si_{un-weathered\ rock}} \times 100$$

206 with: $4Si = Si/4$

207 and the ratio:

208 $$\frac{R^{3+}}{R^{3+} + R^{2+} + M^{+}}$$

209

210 with $M^{+} = Na^{+} + K^{+} + 2Ca^{2+}$; $R^{2+} = Mg^{2+} + Fe^{2+} + Mn^{2+}$; and $R^{3+} = Al^{3+} + Fe^{3+}$. The WIS is
211 used to estimate the weathering intensity by quantifying the loss in silica and the
212 accumulation of the less mobile elements Fe and Al during weathering. Intense weathering
213 corresponds to an important loss in silica, alkaline and alkaline-earth elements during the
214 transformation of primary minerals into clay minerals and relative accumulation of Fe and Al
215 into oxy-hydroxides (i.e. goethite, hematite, gibbsite) and results values of Δ4Si and $R^{3+}/(R^{3+}$,
216 $R^{2+} + M^{+}$) close to 100 %.

217 Elements losses or gains during weathering (tau: τ) were calculated in reference to un-
218 weathered rock chemical composition considering Ti as resistant to chemical weathering
219 (Anderson et al., 2002).

220 $$T_{j,w} = \left(\frac{C_{j,w}.C_{i,uw}}{C_{i,w}.C_{j,uw}}\right) - 1 \qquad (1)$$

221 tau, $\tau_{j,\ w}$ [unitless ratio] is the fraction of the mobile element *j* lost or gained within a
222 weathered rock layer; $C_{j,w}$ is the concentration of element *j* in the weathered rock (*w*) or un-
223 weathered rock (*uw*); $C_{i,uw}$ and $C_{i,w}$ are the concentrations of the immobile element (Ti) in un-

224 weathered rock and weathered rock layer, respectively. Negative values of $\tau_{j,w}$ indicate a loss
225 of the considered element while positive values indicate enrichment relative to the un-
226 weathered rock. Changes in the volume are calculated using the bulk density of in un-
227 weathered rock (*uw*) and weathered rock (*w*). The strain parameter (ε) (Brimhall and Dietrich,
228 1987; Egli and Fitze, 2000; Anderson et al., 2002) is calculated by:

229 $$\varepsilon_{i,w} = \left(\frac{\rho_{uw} \cdot C_{i,uw}}{\rho_{w} \cdot C_{i,w}}\right) - 1 \qquad (2)$$

230 ρ_{uw} and ρ_{w}: the bulk densities of un-weathered rock and weathered rock layers, respectively.
231 Positive values of the strain (ε) indicate an increase of volume (dilation) and negative values a
232 contraction during weathering.
233
234 *2.3.2 Particle size fractionation*
235
236 The samples were fractionated into six particle size fractions: gravels (> 2 mm), coarse sand
237 (200-2000 µm), fine sand (50-200 µm), coarse silt (20-50 µm), fine silt (2-20 µm) and clay
238 fraction (< 2 µm). Un-weathered rock and saprock samples were disaggregated into 1 mol L^{-1}
239 NaCl solution and agitated to separate the secondary minerals present in the porosity without
240 breaking primary ones. The sands and gravels fractions were obtained by sieving. The <50
241 µm fractions were then dispersed into 1 mol L^{-1} NaCl (three saturations) and submitted to
242 ultrasonication. The silts and clay fractions were obtained by sedimentation according to
243 Stockes' law. The clay fractions were then flocculated with addition of $CaCl_2$ and aliquots
244 were subsequently Ca-saturated ($CaCl_2$ 0.5 mol L^{-1}) or K-saturated (KCl 1 mol L^{-1}), and then
245 washed to remove the salt excess.
246 *2.3.3 Mineralogy*
247

Bulk samples, gravels, sand, and coarse silt fractions were ground using a McCrone Micronising Mill. X-ray diffraction (XRD) analyses were performed on randomly oriented powders in the range 2–65° 2θ with steps of 0.025° 2θ and a counting time of 192 s per step using a Bruker D8 Advance diffractometer (Cu Kα radiation, 40 kV and 40 mA) equipped with a Lynx eye detector. Fine silt and clay fractions were analysed from oriented mounts obtained by depositing a small amount of suspension onto glass slides and drying them at room temperature. Ca-saturated samples were analysed by XRD both in an air-dried (AD) state and after ethylene glycol solvation (EG, vapour at 50ºC overnight) using the same equipment in the range 2–35° 2θ with steps of 0.016° 2θ and a counting time of 229 s.

2.3.4 Petrography and Scanning Electron Microscopy

Thin sections (thickness 30 µm) were prepared from un-weathered rock, saprock and saprolite samples after impregnation of the friable samples with bi-component epoxy resin (Araldite ® 2020 or Araldite ® GY 279). The resin for some of them was coloured with a blue dye. The thin sections were polished with silicon carbide and diamond abrasive discs for SEM observations. Petrographic observations were performed using a Nikon Eclipse E600 POL optical microscope under transmitted and polarized light. Images were obtained using the NIS-Elements D 3.0 program. The same thin sections were observed with a Scanning Electron Microscope after carbon coating (SEM JEOL/MP JSM-IT500 15 kV, probe current 1nA, 11mm working distance), equipped with an Energy Dispersive X-ray Spectrometer (EDS, BRUKER X-Flash 4010) allowing microanalysis and element mapping. Images were recorded in Back Scattered Electron mode (BSE) at a resolution 1280 × 960 pixels and a scan time of 40 s to distinguish between phases as the grey levels are correlated to their mean atomic number.

The chemical compositions of the analysed minerals were plotted in a M^+–4Si–R^{2+} ternary diagram also showing the chemical compositions of selected minerals: quartz that plot on the 4Si pole, plagioclases (albite and anorthite) and potassic feldspars (orthoclase) that plot on the line M^+-4Si ($R^{2+} \simeq 0$), biotite, chlorite.

2.4 Bulk density measurements

The bulk density was measured on un-weathered rock and saprock samples by immersion into water according to Flint and Flint (2002). Saprolite and soil samples were too friable to determine bulk density using this method. The samples (several cm^3) were weighted after drying at 110°C for 48h to remove all residual water. The samples were placed into vacuum and progressively immersed into degassed water to fill the porosity with water and stayed immersed for 2-3 weeks to ensure complete saturation of the pores with water. Then the samples were weighed in the saturated state and under immersion in water. This procedure allowed measuring the total volume and subsequently the bulk density (g cm^{-3}) calculations.

3. RESULTS

3.1 Total chemical analyses and weathering indices

The bulk chemical composition in major elements is given in Table 1. The contents in Na_2O + K_2O versus SiO_2 of the un-weathered rock in the TAS diagram (Bas *et al*., 1986) plot in the granodiorite domain. The contents in K_2O and SiO_2 of 3.82 % and of 64.99 %, respectively assign the granodiorite of calco-alkaline series rich in potassium (Peccerillo and Taylor, 1976). The Fe_2O_3 / (Fe_2O_3 + MgO) ratio vs. the content in SiO_2 reveals a magnesian character of the rock. The A/NK ((Al_2O_3 / (Na_2O + K_2O)) versus the A/CNK ratio (Al_2O_3 / (CaO +

298 $Na_2O + K_2O$)) indicates a peraluminous character of the rock with an excess of aluminium
299 that is in agreement with the presence of plagioclase, K-feldspars and biotite.
300 The chemical composition was also converted in molar proportion to calculate two
301 weathering indices (Table 2). The Chemical Index of Alteration (CIA) values range from
302 59.65 % in the un-weathered rock to 60-61 % in the saprock and bottom of the saprolite, to
303 67-68% in the top of the saprolite and grades abruptly to 85.73 % in the soil. These values
304 indicate a progressive chemical weathering with the leaching of alkaline and alkaline-earth
305 cations in saprock and saprolite, larger losses in the top of the saprolite and, important losses
306 and mineralogy dominated by kaolinite in the soil.
307 The chemical composition of the different samples was also plotted in a M^+–4Si–R^{2+} ternary
308 diagram (Figure 2a). The data are aligned along a line going from the composition of the un-
309 weathered granodiorite up to kaolinite (4Si pole). The $R^{3+}/(R^{3+} + R^{2+} + M^+)$ ratio varies
310 between 0.51 in the un-weathered rock and 0.63 in the top of the saprolite and reaches
311 abruptly 0.83 in the soil (Table 2) indicating progressive upward losses in alkaline and
312 alkaline earth cations and conversely a relative accumulation of Fe and Al. The Δ4Si ratio
313 varies between 4.67 % in the bottom of the saprock to 29.31 % in the top of the saprolite and
314 grades abruptly to 56.83 % in the soil also indicating a loss in silica in most weathered
315 samples (Table 2). The plot Δ4Si vs. $R^{3+}/(R^{3+} + R^{2+} + M^+)$ ratios displays the weathering
316 trend of the studied granodiorite along the profile. The two ratios increase simultaneously and
317 progressively in the saprock and the saprolite and sharply in the top of the saprolite and the
318 soil. The values indicate moderate chemical weathering, losses of silica and cations, an
319 accumulation of the less mobile elements and finally mineralogy dominated by kaolinite in
320 the soil. The weathering trend of Viamão granodiorite is like the one calculated from the
321 values of the granodiorite studied by White et al. (2002) also displayed in the Figure 2b.
322 However, the chemical weathering is less intense in the saprolite compared to the samples

studied by White et al. (2002) implying a more progressive and lower intensity chemical weathering.

The element loss (τ) values (Table 3) are negative for almost all alkaline and alkaline-earth and Mn^{2+} cations in the saprock, saprolite and soil layers because of losses of these elements during weathering of biotite and feldspars. Si, Al, and K have a similar trend with values close to 0 in saprock and saprolite which increase in the top of the saprolite and decrease sharply in the soil. This is related to the presence of these elements in the primary and secondary minerals and low chemical weathering. Fe is slightly accumulated in the saprolite and soil by the formation of iron oxides. The trend of the values towards the surface also indicates that weathering intensity is not a linear function of depth, but it exists layers with less weathered samples (ex. Boulders).

The strain (ε) values (Table 3) are close to 0 for saprock and saprolite and of 0.37 for VIA02. This respectively indicates the absence of volume changes during the first stages of weathering and a contraction in the top of the saprolite due to a decrease in mechanical strength resulting from weathering and the fact that mineral grains are no more contiguous.

3.2 Particle size fractionation and mineralogy

The proportion of the particle size fractions are given in Figure 3. The results show that coarse fractions (gravels and sand) are dominant in all samples excepted soil. The silt fractions vary from 2 % in the un-weathered rock to 22 % in the soil. The clay fraction is low in the un-weathered rock (1.3 %), saprock (1.7-3.0 %) and saprolite (1.9-6.5 %) but increases sharply in the soil (39.1%). These features are indicative of a low chemical weathering of the rock in the profile except in the soil layer. The ratio gravel/(sand + silt) (Table 4) that decreases towards the top of the saprolite and the soil reveals the production of sand- and silt-

sized particles by fragmentation of coarse primary mineral (gravel-sized visible with the naked eye) of the rock as described by Frazier and Graham (2000).

Bulk samples

The primary mineralogy of the bulk samples is composed of plagioclases feldspars (albite, anorthite, oligoclase), potassic feldspars (orthoclase), biotite, quartz and iron oxy-hydroxides (Supplementary Figure 2). This mineralogy is similar whatever the weathering stage. The intensity of the peaks of plagioclases and potassic feldspars decreases from the un-weathered rock to the saprolite, compared to quartz peak one, indicating their weathering. In the soil, the abundance of primary minerals sharply decreases. Chlorite is identified only in the un-weathered rock and may correspond to post-magmatic alteration of biotite. Kaolinite is present from the saprock to the soil and the intensity of its peak increases in the soil sample. 2:1 clay minerals are identified in the saprock, the saprolite (GRV09) and in the soil. They will be further identified by analyses of the clay fraction.

Gravels, coarse and fine sands, and coarse silts

The gravels and the coarse sands (not shown) present similar mineralogy composed of plagioclase feldspars (Oligoclase-Andesine), potassic feldspars (orthoclase), biotite, quartz. Their mineralogy is also close to that of the bulk samples. The fine sands present mineralogy close to that of coarse sands but with additional clay minerals (Supplementary Figure 3). Kaolinite (peaks at 7.15 and 3.57 Å) is present in saprock, saprolite, and soil and the intensity and the width of its peaks increase in most weathered samples. The peaks at 10.40 Å, ~ 5.0 Å and ~ 3.33 Å are assigned to weathered biotite, and the peaks at the position between 10 Å and 15 Å indicate mixed-layering between illite and swelling layers (vermiculite or smectite). Their identification will be further detailed on oriented mounts of the clay fraction.

The primary mineralogy of the coarse silts is close to that of the sands (Supplementary Figure 4). The weathered mica is mainly present in the saprock and the bottom of the saprolite. The

373 mixed layers between mica and swelling phases are present in the saprock and saprolite but in
374 low amounts; and their contents increase gradually with weathering as indicated by the
375 increase of the intensity of their peaks compared to that of quartz.
376 *Fine silts*
377 The mineralogy of the fine silts (Figure 4) and of the clay fraction (Figure 5) were obtained
378 from oriented preparations that were recorded both in AD and EG states.
379 The fine silts exhibit peaks with low intensity assigned to primary minerals like plagioclases
380 (4.24 Å, 4.04 Å and 3.19 Å), biotite (10.00 Å, 5.00 Å and 3.33 Å), quartz (4.26 Å and 3.34 Å)
381 indicating they are present in low amounts in these fine fractions that mainly contained
382 minerals resulting from chemical weathering (Figure 4). Chlorite is identified by peaks at
383 14.56, 7.07 Å, 4.72 Å and 3.54 Å that do not displace after EG solvation in the un-weathered
384 granodiorite. Kaolinite is identified by peaks at 7.23 Å 4.47 Å and 3.57 Å that do not shift
385 upon EG treatment. The width of kaolinite peaks increases towards the surface indicating
386 lower crystallinity that is often the case in tropical soils. Kaolinite is the dominant mineral at
387 the top of the saprolite and in the soil. In the un-weathered rock (GRV01) and the saprock
388 (GRV03) a wide peak is observed at 14.56 Å in AD that shifts to 16.34 Å in EG, with
389 harmonics at 8.23 Å and 2.71 Å. In the middle to upper saprolite samples (GRV07, VIA01,
390 VIA03, VIA02, GRV09) the peak positions gradually change to 14.74 Å in AD and 16.71 Å
391 in EG. These peaks correspond to a mixed layer vermiculite/smectite rich in smectite layers
392 that present an increase in smectite proportion towards the surface. In the GRV05, the peak
393 position at 14.56 Å in AD which is identical after EG solvation is attributed to vermiculite. In
394 the un-weathered rock and the saprock, peak positions at 12.87 Å in AD and 14.44 Å in EG
395 with a super-structure at 24.25 Å in AD and 26.5 Å in EG (not shown in figure 4) indicate the
396 presence of an ordered mixed-layer biotite-vermiculite. In the saprolite (samples VIA01 and
397 VIA02), the broad and asymmetric peaks observed respectively at 10.70 Å and 10.34 Å in AD

398 that split into two peaks at Å and 9.81 Å and ~ 3.30 Å in EG are attributed to a partially long-
399 distance ordered (R2-R3) illite-rich illite/smectite mixed layer. In the soil, residual mica is
400 observed by peaks at 9.97 Å, 5.00 Å and 3.33 Å. The saprolite samples VIA03 and VIA02
401 present a third illite/smectite mixed layer with a *001* peak at 12.47 Å in AD and 16.71 in EG,
402 with a slight displacement of the peaks towards lower angles in the surface. The intensity of
403 the peaks of the mixed-layers increases from saprock to saprolite indicating an increase in
404 their abundance.

405 *Clay fractions*

406 The XRD patterns of the clay fractions are shown in Figure 5. Residual plagioclases and
407 quartz are still identified in the clay fraction. Chlorite is identified in the un-weathered rock
408 by peaks at 14.13 Å, 7.07 Å, 4.73 Å, 3.54 Å and 2.83 Å in AD which are not affected by EG
409 solvation. The XRD pattern of the un-weathered rock also exhibits a sharp peak at 14.72 Å in
410 AD that displaces to 15.90 Å and 8.01 Å in EG and that collapses to 10.20 Å upon K
411 saturation attributed to vermiculite/smectite mixed layer.

412 The XRD pattern of the saprock sample (GRV03) presents a peak at 14.78 Å in AD that
413 swells to 16.24 Å in EG with harmonic at 8.14 Å and that collapses to 10.20 Å after K
414 saturation, which is attributed to vermiculite/smectite mixed layers.

415 The vermiculite/smectite mixed layer is present up to the saprolite (VIA02) but with a slight
416 change in peak positions towards small angles indicating an increase of the smectite layers
417 proportion. In the sample VIA01, the swelling is more important with peaks in EG state at
418 16.81 Å and 9.10 Å. In the saprolite (sample GRV09) the peaks are observed at 15.12 Å in
419 AD and 16.77 Å and 8.36 Å in EG. These features are both indicating a progressive
420 transformation of vermiculite into smectite with increasing weathering. The peak at 12.16 Å
421 after K saturation also indicates the presence of a chlorite-smectite or chlorite-vermiculite
422 mixed layer.

Residual mica 9.97 Å, 5.00 Å and 3.33 Å is observed in the top sample of saprolite and in the soil. Finally, kaolinite is identified from saprock up to the soil with broad peaks at à 7.23 Å and 3.57 Å that do not displace upon EG solvation. The intensities of the peaks of kaolinite increase from saprock towards the surface indicating an increase in its proportion. Kaolinite is the dominant mineral in the top of the saprolite and the soil resulting from more advanced chemical weathering.

3.3 Micromorphological and chemical composition of weathered minerals

Un-weathered rock

The un-weathered rock presents phenocrysts of potassic feldspars, plagioclases, biotite, and quartz (Figure 6). Plagioclases display anorthite exsolution lamellae (Figure 6d). The minerals appear with minor chemical alteration but present intergranular and intragranular microcracks. Unaltered biotites in the fresh rock show high order green interference colour and strong dark brown pleochroism (Figure 6a). Some partially chloritized biotites show reduced pleochroism. Iron oxides are observed in the microcracks at the vicinity of the biotites (Figure 6a). Titanite is also observed in some samples, indicating along with chloritized biotite, the occurrence of hydrothermal alteration of the granodiorite protolith after its intrusion. SEM observations of un-weathered rock sample display microcracks at the boundary of the grains and inside plagioclases, K-feldspars, and biotite crystals (arrows Figure 6d-f). The average apertures of the cracks in both minerals are below 5 µm. The mineral grains are contiguous, fracturation did not change the relative position of mineral grains. In biotites and plagioclases the average microcracks aperture is below 5 µm and below 2 µm for K-feldspars.

The chemical compositions of the analysed minerals were plotted in a M^{+}–4Si–R^{2+} ternary diagram (Figure 10a). Plagioclases are plotted between albite and anorthite chemical

448 composition on the line M^{+}-4Si ($R^{2+} \simeq 0$), and potassic feldspars plot on orthoclase average
449 composition. Biotites have the average composition of biotite from granitic rocks, chlorites
450 plot close to the R^{2+} pole because of their content in Fe^{2+} and/or Mg^{2+} and are distributed on a
451 line joining biotite indicating they originate from biotite chloritization. These results agree
452 with XRD data on bulk rock samples.

453 *Saprock*

454 The same minerals are identified in the saprock (GRV05) (Figure 7) with a slightly higher
455 weathering degree. Biotites are the minerals that present the higher changes at this stage of
456 weathering, being expanded along their cleavages forming a network of fissures partially
457 filled with secondary material (Figure 7 a and f). Some plagioclases present dissolutions along
458 twin planes but the majority are not chemically altered but present numerous intragranular
459 and intergranular microcracks of aperture < 20 µm. Quartz does not present any changes in
460 the saprock. SEM observations in the saprock show a larger development of the microcracks
461 network. Plagioclases and K-feldspars exhibit intergranular and intragranular microcracks,
462 and some dissolution pitting (Figure 7 d-f). Biotites present larger pores along cleavages
463 attributed to the expansion of layers. The average aperture of the microcracks is below 20 µm
464 and that of macrocracks of about 150 µm for all minerals. The mineral grains are still joined.
465 The chemical compositions plotted in a M^{+}–4Si–R^{2+} ternary diagram shows the formation of
466 two series of secondary minerals (Figure 10b). The first one is located along the line felspars
467 – 4Si pole and corresponds to the weathering of feldspars to form clay minerals such as
468 smectite and/or kaolinite (4Si pole). The second one is located along with line biotite – 4Si
469 pole that corresponds to the weathering of biotite into vermiculite and smectite as identified in
470 XRD.

471 *Saprolite*

The three analysed samples of saprolite (VIA03, GRV09, GRV10) (Figures 8 and 9) show an upward increase in chemical weathering. Biotite alteration increases as shown by reduced birefringence and pleochroism, and large exfoliations and presence of iron oxy-hydroxides in the cracks. Cracks apertures increase upward and transgranular macropore network form with partial infilling of clay minerals and iron oxides (white in BSE images). In the bottom of the saprolite (VIA03), the porosity is close to that observed in the saprock; but crack apertures increase (Figure 8). Plagioclases are progressively weathered upward, and numerous dissolution pits are observed (Figure 8b). The replacement of plagioclases by kaolinite is pseudomorphic in the saprolite. K-feldspars are partially weathered with dissolution pits and present numerous cracks whose aperture increases upward. Quartz grains remained chemically non-altered but presented numerous microcracks.

The samples GRV09 and GRV10 of the saprolite show a much more developed and connected pore network. Numerous cracks associated with dissolution pits are located in plagioclases and K-feldspars that are filled by secondary material (clay minerals) (Figure 9 a-c, e). The biotites show significant exfoliation (Figure 9d and f) and are surrounded by iron oxides accumulation (white in BSE). Intergranular macrocracks develop and mineral grains are no longer contiguous (Figure 9 a-d). The sample from the top of the saprolite (GRV10) displays an open pore network and the primary minerals are no longer contiguous, except few rare contacts between grains.

Chemical analyses plotted in the M^{+}–4Si–R^{2+} ternary diagram confirm the two weathering sequences observed for saprock (Figure 10c). In the deepest sample of saprolite, biotite crystals present minor chemical alteration and the weathering products plot on a line going from biotite composition in un-weathered rock up to kaolinite through the composition of smectites. Chemical alteration increases upward, the plot is more dispersed for sample GRV09 and are more aligned on the biotite alteration trend for sample GRV10 and converges

497 to kaolinite composition. These results agree with the XRD results and confirm the
498 progressive transformation of biotite into vermiculite, then into smectite by pathways
499 including mixed layers of intermediate composition and finally into kaolinite in the most
500 weathered sample of saprolite. The chemical analyses performed in the dissolution pits of
501 pseudomorphs plagioclases feldspars show two trends. In a first step the analyses plot
502 between the composition of the two end-members of plagioclases (albite and anorthite) and
503 smectites (montmorillonite) (Figure 10d), and in a second step the chemical changes are
504 related to a left shift of the composition that is aligned along a line montmorillonite-4 Si pole
505 (kaolinite) where they converge (Figure 10e).
506 The weathering of feldspars shows two trends: a first trend with low chemical weathering and
507 losses in element and formation of smectites from the elements (Si, Al, Ca, Na) released by
508 the weathering; and a second trend with a higher degree of chemical alteration and losses in
509 elements and formation of kaolinite with the remaining Si and Al (Figure 10f). This might be
510 attributed either to two steps of weathering of feldspars in the saprock and saprolite and/or to
511 the first step of weathering of plagioclases and the second step of weathering of both
512 plagioclases and K-feldspars. This trend is in agreement with XRD data.
513
514 The intensity of chemical mineral weathering, grain fragmentation and connected porosity
515 development increases upward in the saprolite. On the top of the saprolite, the grains are
516 dislodged and rock structure is lost to form pedogenic structure governed by seasonal
517 shrinkage and swelling. Dissolution pits in feldspars create an intergranular micropore
518 network, and biotite expansion increase in chemical weathering which creates an intergranular
519 dense macrocracks network. Total porosity and macroporosity increased upward in saprolite.
520
521 *3.4 Evolution of total porosity*

522

523 The water saturation/immersion estimates the total connected porosity of the samples
524 obtained from bulk and dry density measurements (Table 5). The un-weathered granodiorite
525 has a mean total porosity of 1.73 % that is a common value for fresh granitic rocks (Rossi and
526 Graham, 2010; Mazurier et al. 2016). The total porosity increases upward in the saprock (3.57
527 – 10.5%) with increase physical fragmentation and chemical weathering. The increase is
528 progressive with weathering of biotite and increases sharply with the weathering of feldspars.
529 Total porosity reaches 11 % in the saprolite. The bulk density simultaneously decreases from
530 2.66 kg dm^{-3} in the fresh rock to 2.40 kg dm^{-3} in the top of the saprolite. The grain density is
531 similar in all the layers (2.68-2.71 kg dm^{-3}).

532

533 **4. DISCUSSION**

534

535 *4.1 Weathering intensity*

536 The studied weathering profile presents a thick saprolite (~ 15 m) with limited chemical
537 weathering and a relatively thin more intensely weathered soil (~ 2 m) on the top similar to
538 granitc regolith with stepped topography described in southern California (Wahrhaftig, 1965;
539 Jessup et al., 2011) and in Australia (Hill, 1996). The presence of a thick mantle of gruss is
540 interpreted as differential weathering of granitic bedrocks in the landscape due to
541 chemical/mineralogical composition of the rocks and tilting (Wahrhaftig, 1965; Jessup et al.,
542 2011; Hill, 1996). This hypothesis may be consistent for this region of southern Brazil
543 affected by faulting and tilting due to tectonics. However, with only one weathered profile
544 studied we are not able to discuss about the controlling factor of the presence of the thick
545 mantle of gruss.

546 Calculation of weathering indices like CIA and WIS indicated that chemical weathering is
547 limited in the studied profile. Figure 2 plotting the loss in silica (Δ4Si) versus the relative
548 enrichment in iron and aluminium oxides (ratio $R^{3+}/(R^{3+} + R^{2+} + M^{+})$) shows that the
549 weathering trend of the studied granodiorite is similar to that obtained with the data from the
550 Panola granodiorite weathering profile from Georgia in the USA (White et al. 2002).
551 However, the values of Δ4Si of the most advanced weathered saprolite sample (GRV10) is
552 29.3% and the ratio $R^{3+}/(R^{3+} + R^{2+} + M^{+})$ is 0.63, whereas data from White et al. (2002)
553 (excluding soil values) presented a Δ4Si of 58.1% and a ratio $R^{3+}/(R^{3+} + R^{2+} + M^{+})$ of 0.88
554 (Figure 2). These values imply a lower intensity of weathering for the studied profile in south
555 Brazil compared to Panola granodiorite. In the studied granodiorite, the weathering is
556 progressive and of limited intensity in the saprock and bottom of the saprolite and increases
557 abruptly in the surface soil layer that presents an advanced stage of weathering common for
558 tropical soils. However, it cannot be precluded with the data we have that the soil is originated
559 from an allochtonous deposit at the surface of the saprolite.
560 The silicates in the studied granodiorite thus underwent low chemical weathering, which
561 explains the low percentage of clay fraction formed. There is only a slight increase in clay
562 fraction from 1.3 % in un-weathered rock to 6.5 % in the saprolite (Table 4, Figure 3). Again,
563 the soil layer is distinguished by a sharp increase in clay fraction (39.1 %). The low
564 percentage of clays formed can also be explained by the composition of the granodiorite,
565 which has a high proportion of quartz and plagioclases than biotites and K-feldspars.
566 The amount of clay fraction or clay + silt fraction increases with chemical weathering as
567 indicated by the values CIA, Δ4Si and $R^{3+}/(R^{3+} + R^{2+} + M^{+})$ (Tables 2-5). The rate of silt and
568 clay particles production may be thus used as an indicator of the chemical intensity of
569 weathering in the saprock and the saprolite. Total porosity also increases as a function of clay
570 or clay + silt fractions indicating that physical fragmentation and chemical weathering are

571 responsible to the porosity development during the weathering of the rock. The concomitant
572 increase in porosity, clay, or clay + silt fractions and τMg (Tables 2-5) indicates that the
573 increase/development of porosity in the initial stage of weathering is due to biotite
574 weathering. The value of the total porosity when chemical indices are equal to zero (1.73 %,
575 Table 5) corresponds to the initial porosity of the un-weathered rock that is most probably
576 related to the decompression during its exhumation towards the surface. The increase of
577 porosity is attributed to the pore formation during weathering. The detailed study of the
578 porosity is presented in the companion article (Bonnet et al., submitted) However, due to the
579 small amount of data it is not possible to establish statistical relationships between these
580 parameters.
581 The weathering in the profile from the bottom to the top of the saprolite is not homogeneous
582 due to heterogeneities of the rock composition. This is common in granite/granodiorite
583 weathering profile and with the presence of un-weathered boulders within the soil profile at
584 different depths.
585 The parameters that most explain the weathering intensity are thus the combination of the
586 weathering indices (WIS or CIA) and the production of fine particles such as silt and clays
587
588 *4.2 Weathering processes*
589 With chemical weathering, secondary mineralogy consisting of clay minerals and iron oxy-
590 hydroxides is formed. The clay minerals, identified by X-ray diffraction, mainly consist of
591 chlorite, kaolinite, residual biotite and mixed-layers biotite/vermiculite, vermiculite and
592 vermiculite/smectite with various proportions in both layers and smectite. The abundances of
593 these species vary with increasing weathering intensity: the biotite/vermiculite mixed layers
594 decrease upward while vermiculite/smectite increases. The proportion of smectite in the I/S
595 increases towards the surface. The proportion of kaolinite increases slightly in the saprock and

596 the bottom of the saprolite and increases sharply in the top of the saprolite and the soil. The
597 formation of clay minerals, present in clay and fine silt fractions, is related to the weathering
598 of the primary minerals in the rock. Biotite is the first mineral to weather as often described
599 for granite weathering (Fordham, 1990; Buss et al., 2008; Cassiaux et al., 2006; Fletcher et
600 al., 2006; Sardini et al., 2006; Robert et al., 2003; Rossi and Graham, 2010). A sequence of
601 weathering of the primary minerals of the granodiorite into clay minerals is established based
602 on petrographic observations. Mixed-layers B/V and V/S and then S form by the progressive
603 weathering of biotite (Churchman, 1980; Curmi and Fayolle, 1981; Aurousseau, 1983,
604 Fordham, 1990; Aoudjit et al., 1995; 1996, Egli et al., 2001; Wilson, 2004) Kaolinite forms in
605 a first step by the weathering of plagioclases and a second step by the transformation of the
606 weathering products of biotite (Fordham, 1990; Wilson, 2004, Churchman and Lowe, 2012).
607 The weathering of biotite and the formation of swelling minerals may play an important role
608 in the fragmentation of the saprock by shrink-swell activity as described by Frazier and
609 Graham (2000). The expansion of biotite and the formation of swelling clay minerals in the
610 incipient weathering of granodiorite control the development of porosity that increases
611 hydraulic conductivity of the weathered rock and larger introduction of water that is
612 responsible for the weathering of plagioclases and K-felspars and the large increase in
613 porosity in the top saprolite.
614 Future work will analyse the opening of the pores during weathering (Bonnet *et al*., Submitted
615 which likely controls the development of the weathering.
616

617 **5. CONCLUSION**

618 The weathering intensity estimated by the production of fine particles of the silt (15.10 % in
619 top saprolite) and clay (6.51 % in top saprolite) size fractions as well as by chemical indices
620 (saprolite (CIA = 68, Δ4Si = 29.31 %) indicated a low to chemical weathering of the

granodiorite. The mineral sequence of weathering is like that commonly described for granitic rocks. Biotite is the first mineral to weather progressively into vermiculite with intermediate mixed layers. Biotite expansion is responsible for the opening of the porosity and subsequently the weathering of plagioclases and K-feldspars into kaolinite. Total porosity largely increases from 1.73 % in the un-weathered rock to 11.03 % in the top saprolite. Porosity of the un-weathered rock and the progressive opening of the rock is likely to control chemical weathering and deserve future works.

ACKNOWLEDGMENTS

The authors acknowledge financial support from the European Union (ERDF) and "Région Nouvelle Aquitaine". The authors acknowledge the Department of Geosciences-Instituto de Geociências from the Universidade Federal do Rio Grande do Sul, Brazil for assistance during field work and sampling.

6. REFERENCES

Anderson, S.P., Dietrich, W.E., Brimhall, G.H., 2002 Weathering profiles, mass-balance analysis, and rates of solute loss: Linkages between weathering and erosion in a small, steep catchment. GSA Bulletin, 114, 1143–1158.

Aoudjit, H., Elsass, F., Righi, D., Robert, M. 1996. Mica weathering in acidic soils by analytical electron microscopy. Clay Minerals, 31, 319-332.

Aoudjit, H., Robert, M., Elsass, F., Curmi, P., 1995. Detailed study of smectite genesis in granitic saprolites by analytical electron microscopy. Clay Minerals, 30, 135-147.

644 Aurousseau, P., Curmi, P., Bouille, S., Charpentier, S., 1983. Les vermiculites hydroxy-
645 alumineuses du Massif Armoricain (France). Approches minéralogique, microanalytique et
646 thermodynamique. Geoderma, 31, 17-40.
647 Bazilevskaya, E., Lebdeva, M., Pavich, M., Rother, G., Parkinson D., Cole D., Brantley S. L.,
648 2013. Where fast weathering creates thin regoliths and slow weathering creates thick
649 regoliths. Earth Surf. Processes Landforms. http://dx.doi.org/10.1002/esp.3369.
650 Bazilevskaya, E., Rother, G., Mildner, D.F.R, Pavich, M., Cole D., Bhatt, M., Jin, L., Steefel,
651 C.I., Brantley S.L., 2015. How Oxidation and Dissolution in Diabase and Granite Control
652 Porosity during Weathering. Soil Sci. Soc. Am. J. 79:55–73 doi:10.2136/sssaj2014.04.0135
653 Bonnet, M., Caner, L., Siitari-Kauppi, M., Mazurier, A., Mexias, A. S., Dani, N., Sardini, P.
654 Weathering of Viamão granodiorite, south Brazil: Part 2 – initial porosity of un-weathered
655 rock control porosity development. Submitted as companion paper.
656 Brantley, S. L., 2010. Weathering: Rock to regoliths. Nature Geoscience, 3, 305 – 306.
657 Brantley, S.L., Lebedeva, M., Bazilevskaya, E., 2014. Relating weathering fronts for acid
658 neutralization and oxidation to pCO_2 and pO_2. In: Holland, H.D., Turekian, K.K. (Eds.),
659 Treatise on geochemistry. 2nd ed. Elsevier, Oxford. P. 327–352.
660 Brimhall, G.H., Dietrich, W.E., 1987. Constitutive mass balance relations between chemical
661 composition, volume, density, porosity, and strain in metasomatic hydrochemical systems –
662 results on weathering and pedogenesis. Geochim. Cosmochim. Acta 51, 567–587.
663 Buss, H.L., Sak, P.B., Webb, S.M., Brantley, S.L., 2008. Weathering of the Rio Blanco quartz
664 diorite, Luquillo Mountains, Puerto Rico: coupling oxidation, dissolution, and fracturing.
665 Geochim. Cosmochim. Acta 72, 4488–4507.
666 Buss, H.L., Lara, M.C., Moore, O.W., Kurtz A.K., Schulz, M.S., White A.F., 2017.
667 Lithological influences on contemporary and long-term regoliths weathering at the Luquillo
668 Critical Zone Observatory. Geochimica et Cosmochimica Acta, 196, 224-251.

669 Carignan, J., Hild, P., Mevelle, G., Morel, J., and Yeghicheyan, D., 2001. Routine Analyses
670 of Trace Elements in Geological Samples using Flow Injection and Low Pressure On-Line
671 Liquid Chromatography Coupled to ICP-MS: A Study of Geochemical Reference Materials
672 BR, DR-N, UB-N, AN-G and GH. Geostandards Newsletter, 25, 187–198.
673 Cassiaux, M., Proust, D. Siitari-Kauppi, M. Sardini, P., Leutsch, Y., 2006. Clay minerals
674 formed during propylitic alteration of a granite and their influence on primary porosity: A
675 multi-scale approach. Clays Clay Miner. 54:541–554.
676 Churchman, G.J., 1980. Clay minerals formed from micas and chlorites in some New Zealand
677 soils. Clay Minerals 15, 59-76.
678 Churchman, G.J., Lowe, D.J., 2012 Alteration, formation, and occurrence of minerals in
679 Soils, in Huang, P.M., Li, Y, Sumner, M.E. (eds.), Handbook of Soil Sciences. 2nd edition.
680 Vol. 1: Properties and Processes. CRC Press (Taylor and Francis), Boca Raton, FL, pp.2001-
681 2072.
682 Curmi, P., Fayolle, M. 1981. Microscopic characterization of weathering in granitic saprolite,
683 in Bidsom E.B.A. (ed.), Submicroscopy of soils and weathered rocks. Centre for
684 Agricultural Publishing and Documentation, Wageningen, pp. 249-270.
685 Eggleton, R.A., Buseck, P.R., 1980. High-resolution electron microscopy of feldspar
686 weathering. Clays and Clay Minerals, 28,173 -178
687 Egli, M., Fitze, P., 2000. Formulation of pedogenic mass balance based on immobile
688 elements: a revision. Soil Sci. 165, 437–443.
689 Egli, M., Mirabella, A., Fitze, P., 2001. Clay mineral formation in soils of two different
690 chronosequences in the Swiss Alps. Geoderma, 104, 145-175.
691 Fletcher, R.C., H.L. Buss, Brantley, S.L., 2006. A spheroidal weathering model coupling
692 porewater chemistry to soil thicknesses during steadystate denudation. Earth Planet. Sci.
693 Lett. 244:444–457. Doi:10.1016/j.epsl.2006.01.055

694 Flint, L.E., Flint, A.L. 2002. Porosity, in: Dane, J.H., Topp, G.C. (Eds.), Methods of Soil
695 Analysis: Part 4 Physical Methods. SSSA Book Series, 5.4, Soil Science Society of
696 America, Madison, WI, pp. 241–254.
697 Fordham, A.W., 1990. Weathering of biotite into dioctahedral clay minerals. Clay Minerals,
698 25, 51-63.
699 Frazier, C.S., Graham, R.C., 2000. Pedogenic transformation of fractured granitic bedrock,
700 southern California: Soil Science Society of America Journal, v. 64, p. 2057–2069.
701 Graham, R.C., Anderson, M.A., Sternberg, P.D., Tice, K.R., Schoeneberger, P.J., 1997.
702 Morphology, Porosity, and Hydraulic Conductivity of Weathered Granitic Bedrock and
703 Overlying Soils. Soil Science Society of America Journal, 61, 516-522.
704 Graham, R.C., Rossi, A.M., Hubbert, K.R., 2010. Rock to regolith conversion: producing
705 hospitable substrates for terrestrial ecosystems. GSA Today 20, 4–9.
706 Gunnell, Y., Louchet, A., 2000. The influence of rock hardness and divergent weathering on
707 the interpretation of apatite fission track denudation rates. Evidence from charnockites in
708 South India and Sri Lanka. Zeitschrift für Geomorphologie, 44, 33-57.
709 Hill, S.M., 1996. The differential weathering of granitic rocks in Victoria, Australia. Journal
710 of Australian Geology & Geophysics, 16, 271-276.
711 Hochella, M.F., Banfield, J.F., 1995. Chemical weathering of silicates in nature: a
712 microscopic perspective with theoretical considerations. Pp. 353-406 in: Chemical
713 Weathering Rates of Silicate Minerals (A.F. White & S.L. Brantley, editors). Reviews in
714 Mineralogy, 31, Mineralogical Society of America.
715 Hoke, G. D., Turcotte, D.L., 2002. Weathering and damage. J. Geophys. Res.,107(B10),
716 2210, doi:10.1029/2001JB001573
717 Hoke, G.D., Turcotte, D.L., 2004. The weathering of stones due to dissolution. Environmental
718 Geology, 46, 305–310.

719 Jessup, B. S., Hahm, W. J., Miller, S. N., Kirchner, J. W., Riebe, C. S., 2011. Landscape
720 response to tipping points in granite weathering: The case of stepped topography in the
721 Southern Sierra Critical Zone Observatory. Appl. Geochem. 48-50.
722 doi:10.1016/j.apgeochem.2011.03.026
723 Jones D. P., Graham R.C., 1993. Water-holding characteristics of weathered granitic rock in
724 chaparral and forest ecosystems. Soil Science Society of America Journal 57: 256–261
725 Lee, M.R., Parsons, I., 1995. Microtextural controls of weathering of perthitic alkali feldspars.
726 Geochimica et Cosmochimica Acta, 59, 21, 4465-4488.
727 Lee, M.R., Hodson, M.E., Parsons, I., 1998. The role of intragranular microtextures and
728 microstructures in chemical and mechanical weathering: direct comparisons of
729 experimentally and naturally weathered alkali feldspars. Geochimica et Cosmochimica Acta,
730 62, 2771-2788.
731 Mazurier, A., Sardini, P., Rossi, A.M., Graham, R.C., Hellmuth, K.-H., Parneix, J.-C., Siitari-
732 Kauppi, M., Voutilainen, M., Caner, L., 2016. Development of a fracture network in
733 crystalline rocks during weathering: Study of Bishop Creek chronosequence using X-ray
734 computed tomography and ^{14}C-PMMA impregnation method. Bulletin, 128, 1423–1438.
735 Meunier, A., Sardini, P., Robinet, J.C., Prêt, D., 2007. The petrography of weathering
736 processes: facts and outlooks. Clay Minerals, 42, 415–435.
737 Meunier, A., Caner, L., Hubert, F., Albani, A.E., Prêt, D., 2013. The weathering intensity
738 scale (WIS): An alternative approach of the Chemical Index of Alteration (CIA). American
739 Journal of Science, 313, 113–143.
740 Navarre-Sitchler A., Steefel C. I., Yang L., Tomutsa, L., 2009. Evolution of porosity and
741 diffusivity associated with chemical weathering of a basalt clast. J. Geophys. Res. Earth
742 Surf. 114, F02016.

743 Navarre-Sitchler, A., Cole, D. R., Rother, G., Jin, L., Buss, H.L., Brantley S.L., 2013.
744 Porosity and surface area evolution during weathering of two igneous rocks. Geochimica et
745 Cosmochimica Acta 109, 400–413.
746 Navarre-Sitchler, A., Brantley, S.L., Rother, G., 2015. How Porosity Increases During
747 Incipient Weathering of Crystalline Silicate Rocks. Reviews in Mineralogy and
748 Geochemistry 80, 331–354. https://doi.org/10.2138/rmg.2015.80.10
749 Nesbitt, H.W., Young, G.M., 1982. Early Proterozoic climates and plate motions inferred
750 from major element chemistry of lutites. Nature 299, 715–717.
751 Peccerillo, A., Taylor, S., 1976. Geochemistry of Eocene calc-alkaline volcanic rocks from
752 the Kastamonu area, northern Turkey. Contributions to mineralogy and petrology, 58, 63–
753 81.
754 Philipp, R., Nardi, L., Machado, R., 1998. O Magmatismo Granítico Neoproterozóico tardi a
755 pós-colisional da região de Porto Alegre, RS. Contribuição ao estudo dos granitos e rochas
756 correlatas, 129–152.
757 Philipp, R.P., Machado, R., Nardi, L.V.S., Lafon, J.M., 2002. O magmatismo granítico
758 Neoproterozóico do Batólito Pelotas no sul do Brasil: novos dados e revisão da
759 geocronologia regional. Brazilian Journal of Geology, 32, 277–290.
760 Robert, R., Sardini, P., Sammartino, Dubois, C., Guillot, L., Rossy, M., Gaviglio, P., Siitari-
761 Kauppi, M., 2003. Porosity changes in a granite close to quarry faces: identification from
762 ^{14}C-PMMA autoradiographs and mineralogical cartographies. The European Physical
763 Journal – Applied Physics, 21, 127–136.
764 Rossi, A.M., Graham, R.C., 2010. Weathering and porosity formation in subsoil granitic
765 clasts, Bishop Creek moraines, California. Soil Science Society of America Journal, 74,
766 172–185.

767 Sardini, P., Siitari-Kauppi, M., Beaufort, D., Hellmuth, K.-H., 2006. On the connected
768 porosity of mineral aggregates in crystalline rocks. American Mineralogist, 91, 1069– 1080.
769 Siitari-Kauppi, M., Lindberg, A., Hellmuth, K.H., Timonen, J., Väätäinen, K., Hartikainen, J.,
770 Hartikainen, K., 1997. The effect of microscale pore structure on matrix diffusion. A site-
771 specific study on tonalite. J. Contaminant Hydrology, 26, 147–153.
772 Souza, P.A., Marques-Toigo, M., 2005. Progress on the palynostratigraphy of the Permian
773 strata in Rio Grande do Sul State, Paraná Basin, Brazil Anais da Academia Brasileira de
774 Ciências - Annals of the Brazilian Academy of Sciences, 77, 353-365.
775 Sternberg, P.D., Anderson, M.A., Graham, R.C., Beyers, J.L., Tice, K.R., 1996. Root
776 distribution and seasonal water status in weathered granitic bedrock under chaparral:
777 Geoderma, v. 72, p. 89–98, doi: 10.1016/0016-7061(96)00019-5.
778 Turner, B.F., Stallard, R.F., Brantley, S.L., 2003. Investigation of in situ weathering of quartz
779 diorite bedrock in the Rio Icacos basin, Luquillo Experimental Forest, Puerto Rico:
780 Chemical Geology, v. 202, p. 313–341, doi: 10.1016/j.chemgeo.2003.05.001.
781 Turner, B.F., Stallard, R.F., Brantley, S.L., 2003. Investigation of in situ weathering of quartz
782 diorite bedrock in the Rio Icacos basin, Luquillo Experimental Forest, Puerto Rico.
783 Chemical Geology, 202, 313–341.
784 Twidale, C.R., 1982. The Evolution of Bornhardts: The nature of these dramatic landforms
785 that rise abruptly from flat plains is now beginning to be more fully understood. American
786 Scientist, 70, 268–276.
787 Velde, B., Meunier, A., 2008. The Origin of Clay Minerals in Soils and Weathered Rocks.
788 Springer, 407 pp.
789 Wahrhaftig, C., 1965. Stepped topography of southern Sierra Nevada, California. Geol. Soc.
790 Am. Bull. 76, 1165-1189.

White, A.F., Blum, A.E., Schulz, M.S., Huntington, T.G., Peters, N.E., Stonestrom, D.A., 2002. Chemical weathering of the Panola Granite: Solute and regoliths elemental fluxes and the weathering rate of biotite. Water Rock Interactions, Ore Deposits, and Environmental Geochemistry: A Tribute to David A. Crerar, 37–59.

Wilson, M.J., 2004. Weathering of the primary rock-forming minerals: processes, products and rates. Clay Minerals, 39, 233–266.

Figures Captions

Figure 1: (a) Simplified geological map of Rio Grande do Sul state in Brazil (modified from Souza and Marques-Toigo, 2005). (b) Geological map of the region of Porto Alegre with location of the studied weathering profile (modified from Philipp et al., 1998).

Figure 2: Chemiographic projections of the total chemical compositions of the studied samples (dots) and the granodiorite samples from White et al. (2002) (square) in a) ternary diagram 4Si-M^+-R^{2+} and in b) diagram Δ4Si versus R^{3+} / (R^{3+} + R^{2+} + M^+) to determine the weathering intensity scale (WIS). $M^+ = Na^+ + K^+ + 2Ca^{2+}$; $R^{2+} = Mg^{2+} + Mn^{2+}$; and $R^{3+} = Al^{3+} + Fe^{3+}$ in cationic molar proportions (Meunier et al., 2013).

Figure 3: Particle size distribution of the samples at different stage of weathering.

Figure 4: X-ray diffraction patterns of the 2 – 20 µm fraction size on oriented mounts in air-dried (AD) and ethylene-glycol (solvated state (EG)) of the samples at different stage of weathering. The percentage of each fraction size is also given.

Figure 5: X-ray diffraction patterns of the < 2 µm fraction size on oriented mounts in air-dried (AD) and ethylene-glycol (solvated state (EG)) of the samples at different stage of weathering. The percentage of each fraction size is also given.

Figure 6: Photographs of un-weathered rock (sample GRV01) under optical microscopy: a) biotite (Bt), K-feldspar (Kf), plagioclase (Pl), anorthite (An), quartz (Qtz) and iron oxides (Ox) and titanite (or sphene: Ti). Biotites are chlotitized (XPL; Mx4); b) plagioclases with altered and fissured core (PPL; Mx2); c) plagioclases, chloritized biotites and quartz (PPL; Gx4). Scanning electron (SEM) micrographs in backscattered electron (BSE) mode: d) plagioclases with intergranular microcracks; e and f) intra and intergranular microcracks through biotites, plagioclases, K-feldspars, and quartz. PPL = Plane Polarized Light; XPL = Cross Polarized Light; M = Magnification.

Figure 7: Photographs of the saprock (sample GRV05) under optical microscopy: a and b) exfoliated biotites and plagioclases with dissolution pits, only cracks between grains exist (XPL; Mx2); c) weathered plagioclases K-feldspars with intragranular cracks (PPL; Mx2). SEM images in BSE mode: d) inter- and intragranular cracks within biotites, plagioclases, K-feldspars, and quartz; e and f) partly exfoliated biotite and dissolution pits in feldspars, Ti-oxides (Ti).

Figure 8: Photographs of the saprolite (sample VIA03) under optical microscopy: a) exfoliated biotites with iron oxy-hydroxide accumulations (XPL); b) plagioclases with dissolution pits and pseudomorphosed replacement with alteration products, only cracks between grains exist (PPL; Mx2). SEM images in BSE mode: c) partly exfoliated biotite and

839 feldspar with intragranular crack; d) inter- and intragranular cracks within K-feldspar; e and
840 f) exfoliated biotite with micro and macrocracks along cleavages.
841
842 **Figure 9:** Photographs of saprolite (sample GRV09) under optical microscopy: a) weathered
843 plagioclases and biotite with open porosity (XPL); b) weathered K-felspar and open
844 macrocracks between quartz (PPL). SEM images in BSE mode: c) weathered K-felspar with
845 dissolution pits filed by clay minerals and macrocrack crossing the mineral grain; d and f)
846 exfoliated biotite and clay minerals; e) same weathered K-feldspars than b showing
847 macrocracks and porous mineral grain.
848
849 **Figure 10:** Chemiographic projections of the chemical compositions of the minerals obtained
850 with the SEM EDS probe in the $4Si - M^{+} - R^{2+}$ ternary diagram.
851
852
853 **Tables Captions**
854
855 **Table 1:** Bulk chemical composition in major elements (wt % oxides)
856
857 **Table 2:** Calculation of weathering indices
858
859 **Table 3:** Element loss/gains
860
861 **Table 4:** particle size distribution of the samples
862
863 **Table 5:** Porosity and density measurements obtained by water immersion method

(a)

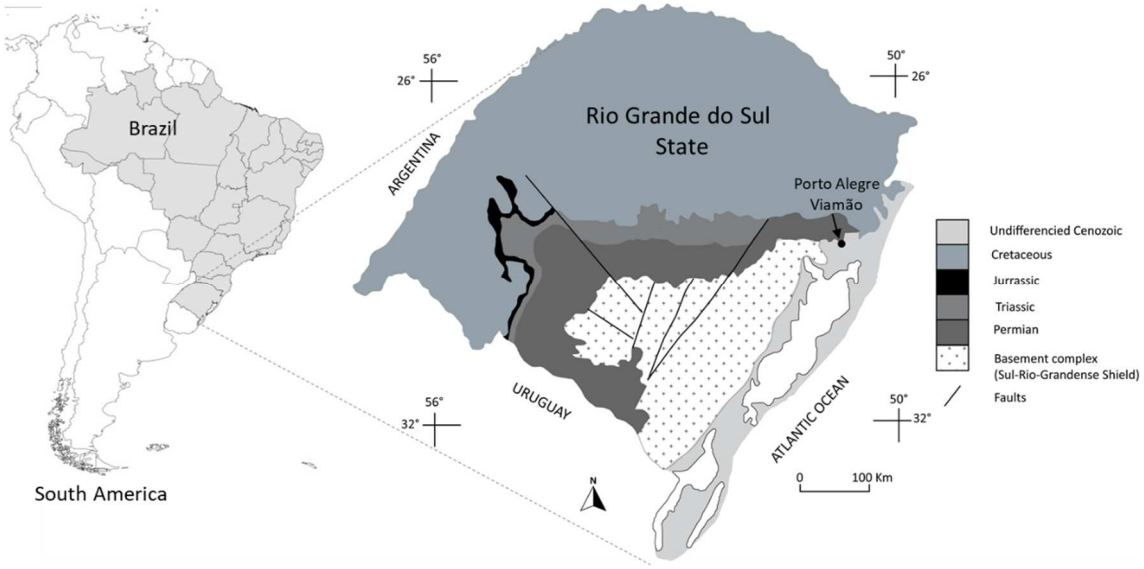

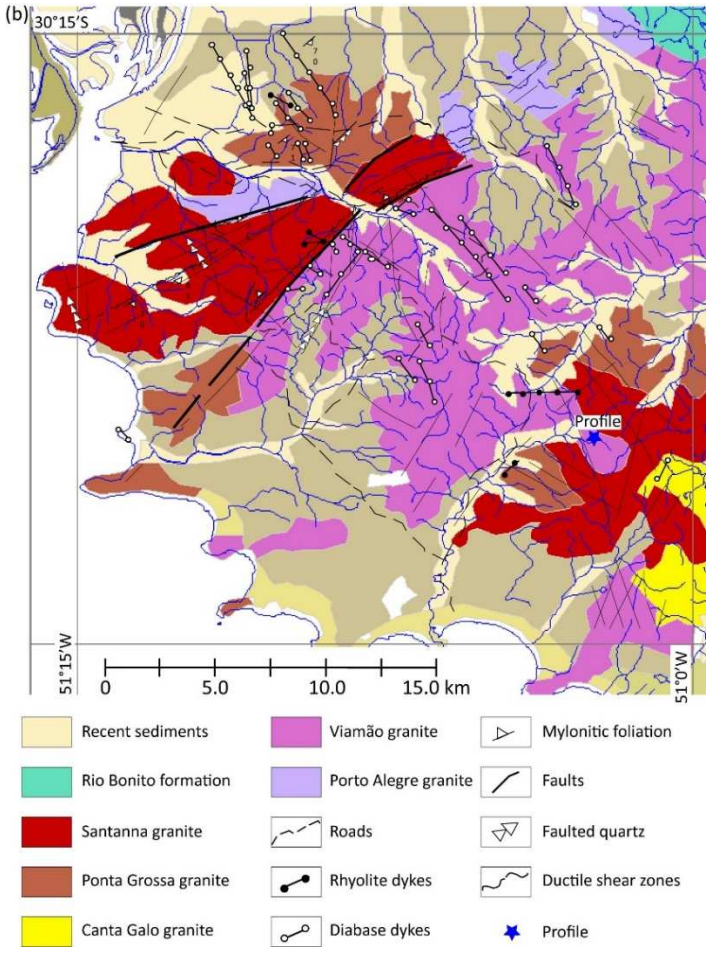

Figure 1: (a) Simplified geological map of Rio Grande do Sul state in Brazil (modified from Souza and Marques-Toigo, 2005). (b) Geological map of the region of Porto Alegre with location of the studied weathering profile (modified from Philipp et al., 1998).

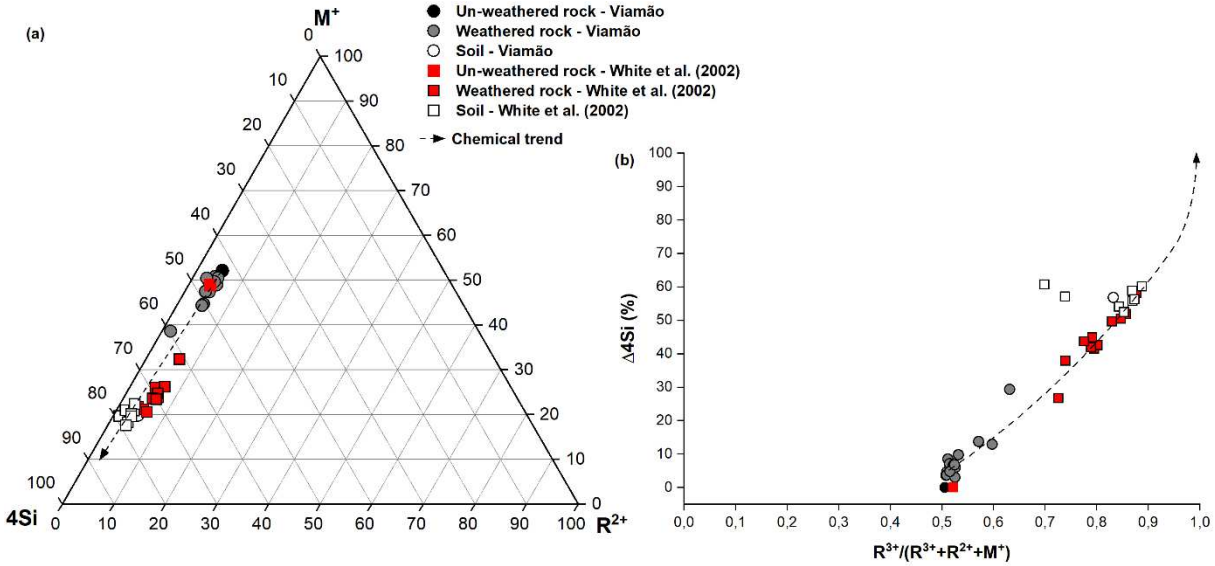

Figure 2: Chemiographic projections of the total chemical compositions of the studied samples (dots) and the granodiorite samples from White et al. (2002) (square) in a) ternary diagram 4Si-M^+-R^{2+} and in b) diagram Δ4Si versus R^{3+} / (R^{3+} + R^{2+} + M^+) to determine the weathering intensity scale (WIS). $M^+ = Na^+ + K^+ + 2Ca^{2+}$; $R^{2+} = Mg^{2+} + Mn^{2+}$; and $R^{3+} = Al^{3+} + Fe^{3+}$ in cationic molar proportions (Meunier et al., 2013).

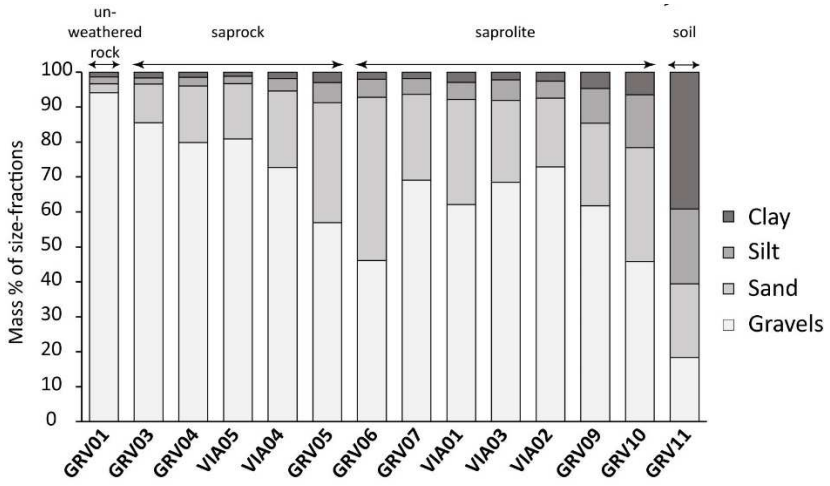

Figure 3: Particle size distribution of the samples at different stage of weathering.

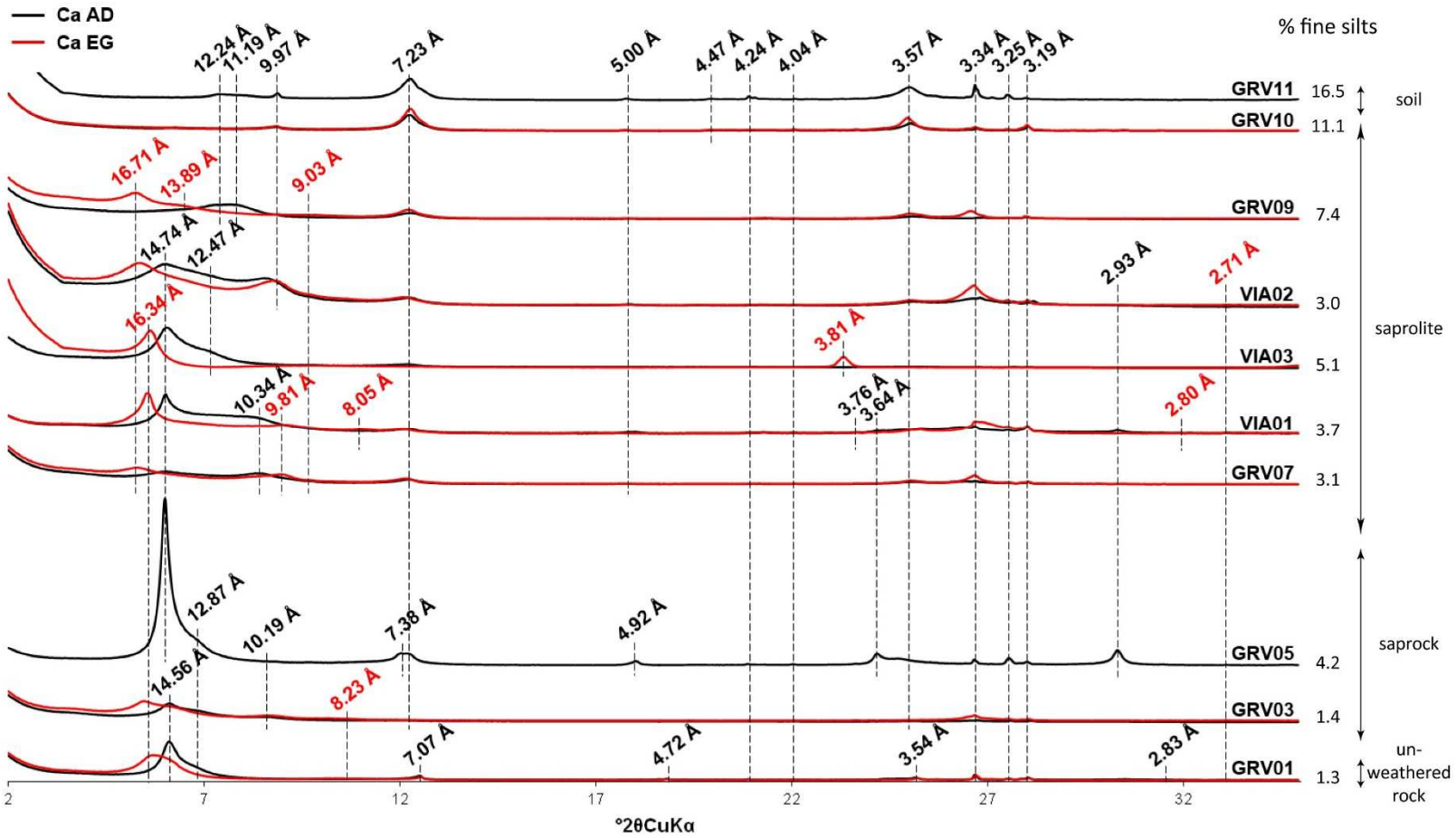

Figure 4: X-ray diffraction patterns of the 2 – 20 µm fraction size on oriented mounts in air-dried (AD) and ethylene-glycol (solvated state (EG)) of the samples at different stage of weathering. The percentage of each fraction size is also given.

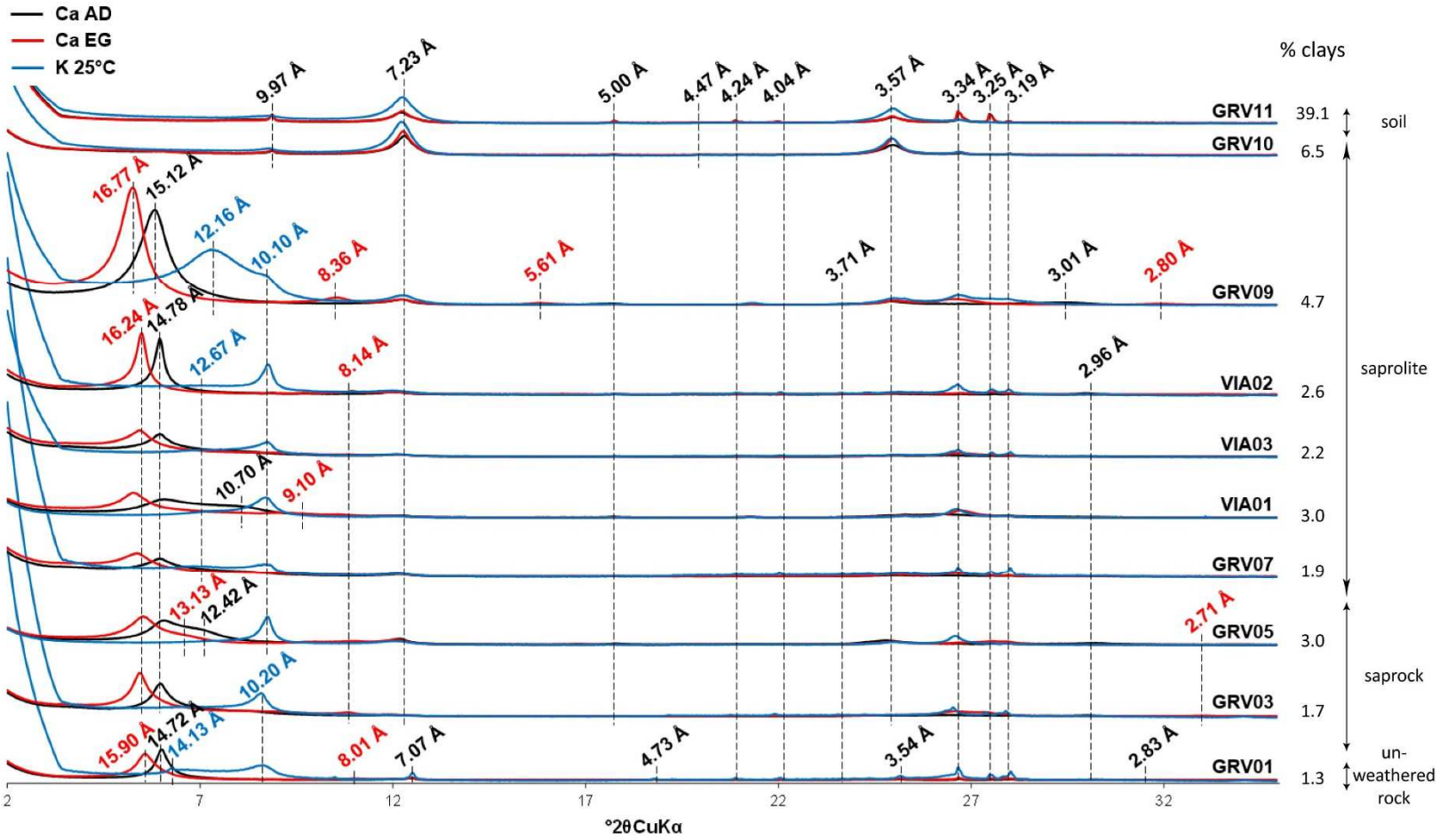

Figure 5: X-ray diffraction patterns of the < 2 µm fraction size on oriented mounts in air-dried (AD) and ethylene-glycol (solvated state (EG)) of the samples at different stage of weathering. The percentage of each fraction size is also given.

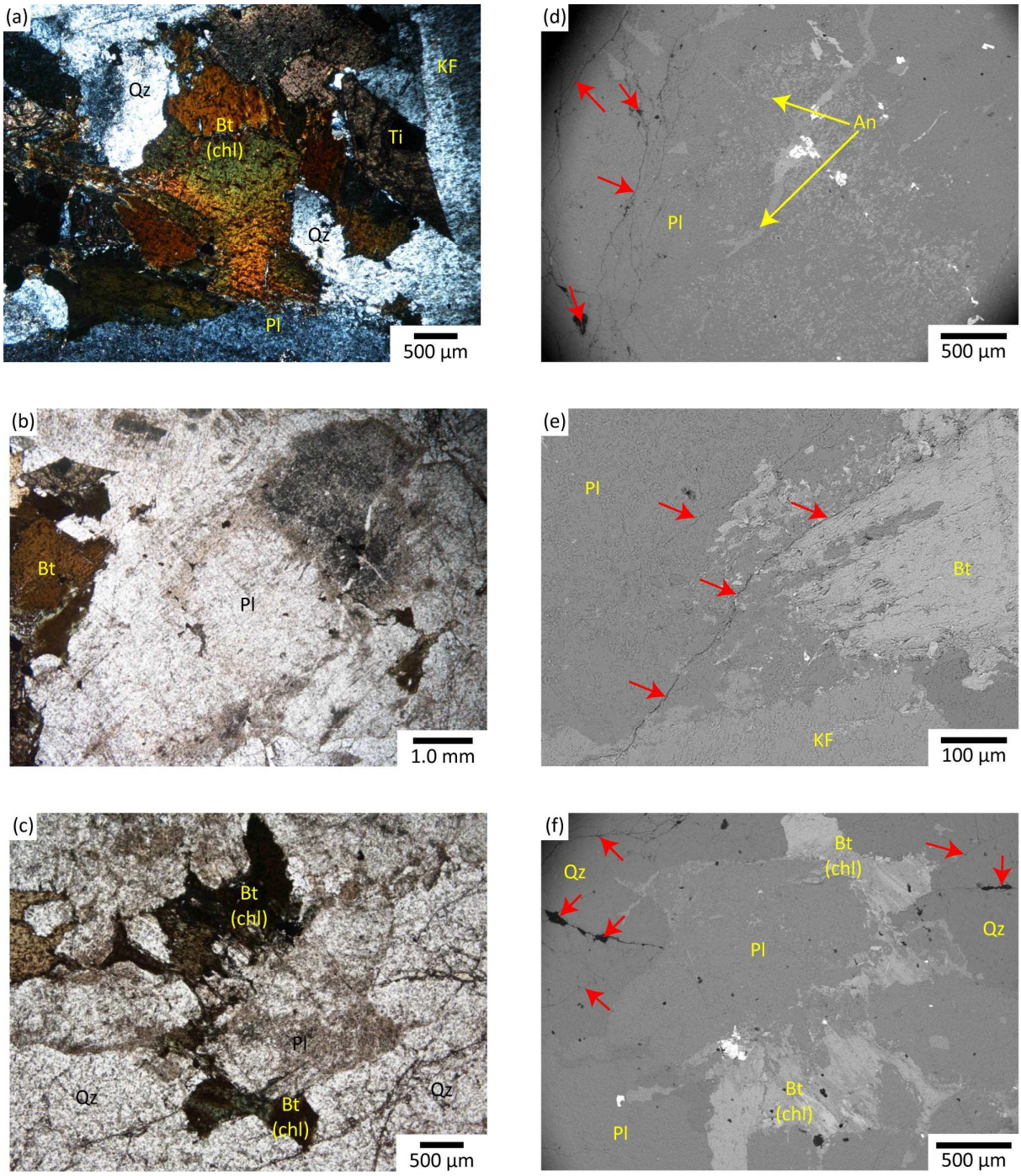

Figure 6: Photographs of un-weathered rock (sample GRV01) under optical microscopy: a) biotite (Bt), K-feldspar (Kf), plagioclase (Pl), anorthite (An), quartz (Qtz) and iron oxides (Ox) and titanite (or sphene: Ti). Biotites are chlotitized (XPL; Mx4); b) plagioclases with altered and fissured core (PPL; Mx2); c) plagioclases, chloritized biotites and quartz (PPL; Gx4). Scanning electron (SEM) micrographs in backscattered electron (BSE) mode: d) plagioclases with intergranular microcracks; e and f) intra and intergranular microcracks through biotites, plagioclases, K-feldspars, and quartz. PPL = Plane Polarized Light; XPL = Cross Polarized Light; M = Magnification.

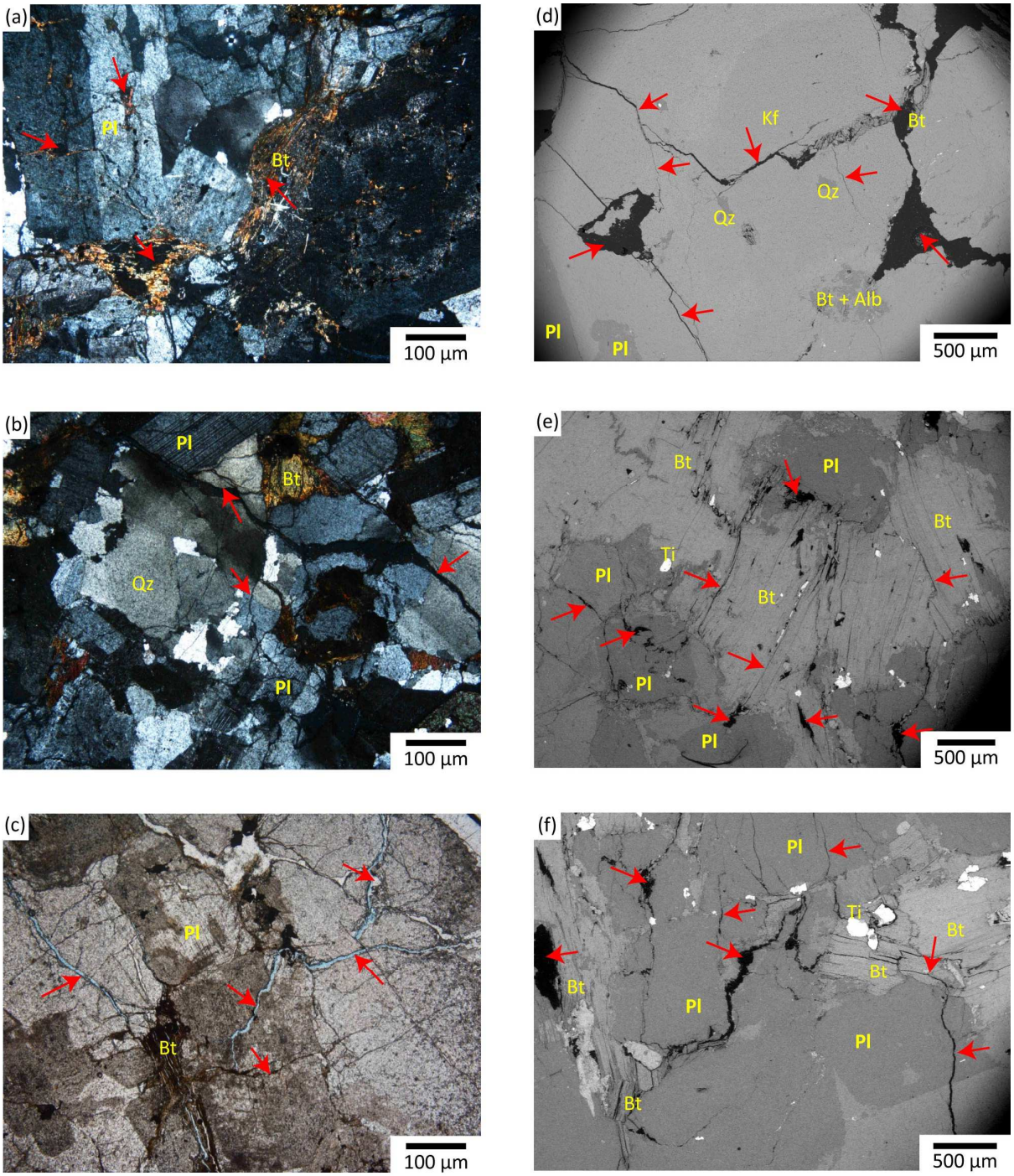

Figure 7: Photographs of the saprock (sample GRV05) under optical microscopy: a and b) exfoliated biotites and plagioclases with dissolution pits, only cracks between grains exist (XPL; Mx2); c) weathered plagioclases K-feldspars with intragranular cracks (PPL; Mx2). SEM images in BSE mode: d) inter- and intragranular cracks within biotites, plagioclases, K-feldspars, and quartz; e and f) partly exfoliated biotite and dissolution pits in feldspars, Ti-oxides (Ti).

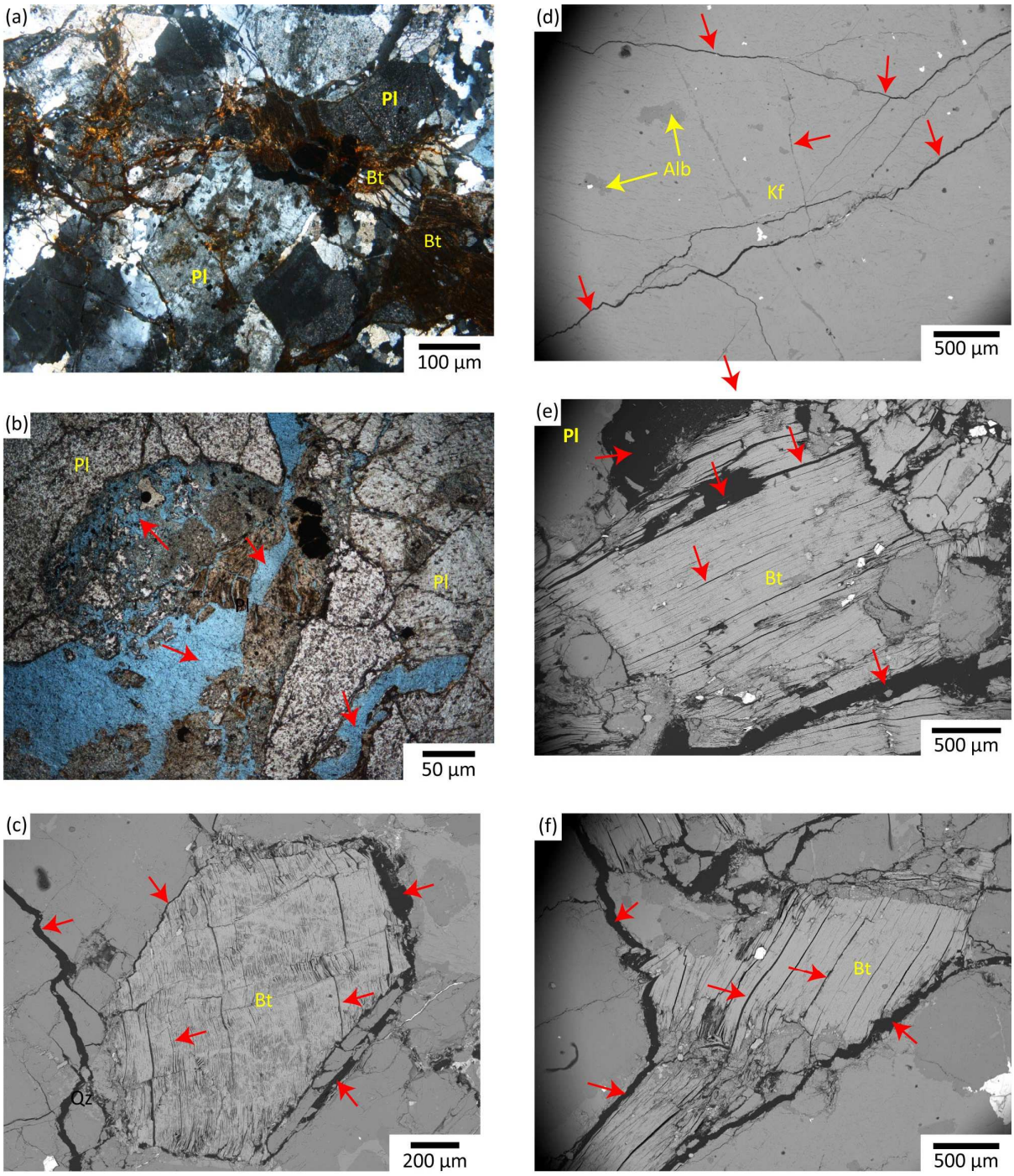

Figure 8: Photographs of the saprolite (sample VIA03) under optical microscopy: a) exfoliated biotites with iron oxy-hydroxide accumulations (XPL); b) plagioclases with dissolution pits and pseudomorphosed replacement with alteration products, only cracks between grains exist (PPL; Mx2). SEM images in BSE mode: c) partly exfoliated biotite and feldspar with intragranular crack; d) inter- and intragranular cracks within K-feldspar; e and f) exfoliated biotite with micro and macrocracks along cleavages.

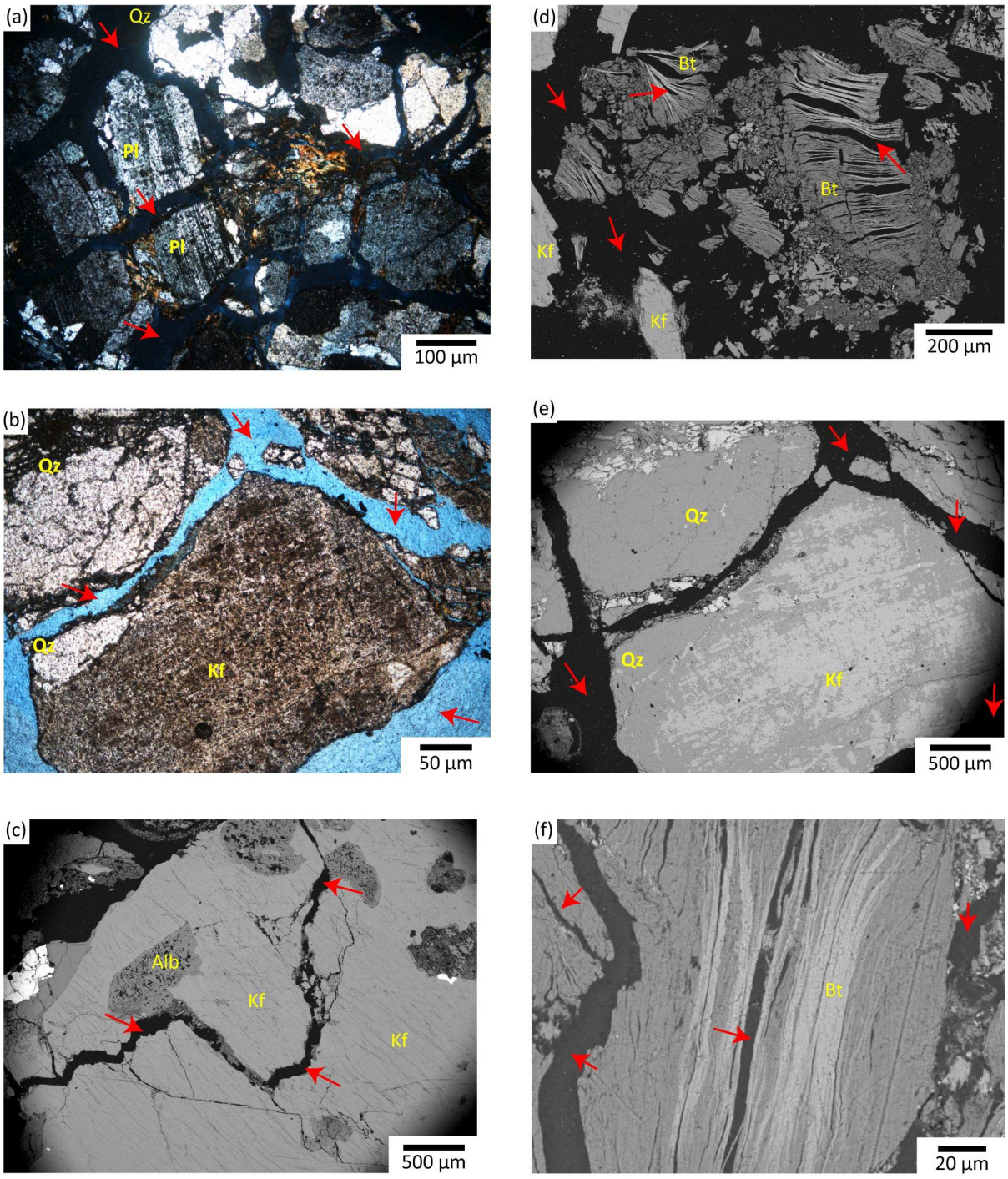

Figure 9: Photographs of saprolite (sample GRV09) under optical microscopy: a) weathered plagioclases and biotite with open porosity (XPL); b) weathered K-felspar and open macrocracks between quartz (PPL). SEM images in BSE mode: c) weathered K-felspar with dissolution pits filed by clay minerals and macrocrack crossing the mineral grain; d and f) exfoliated biotite and clay minerals; e) same weathered K-feldspars than b showing macrocracks and porous mineral grain.

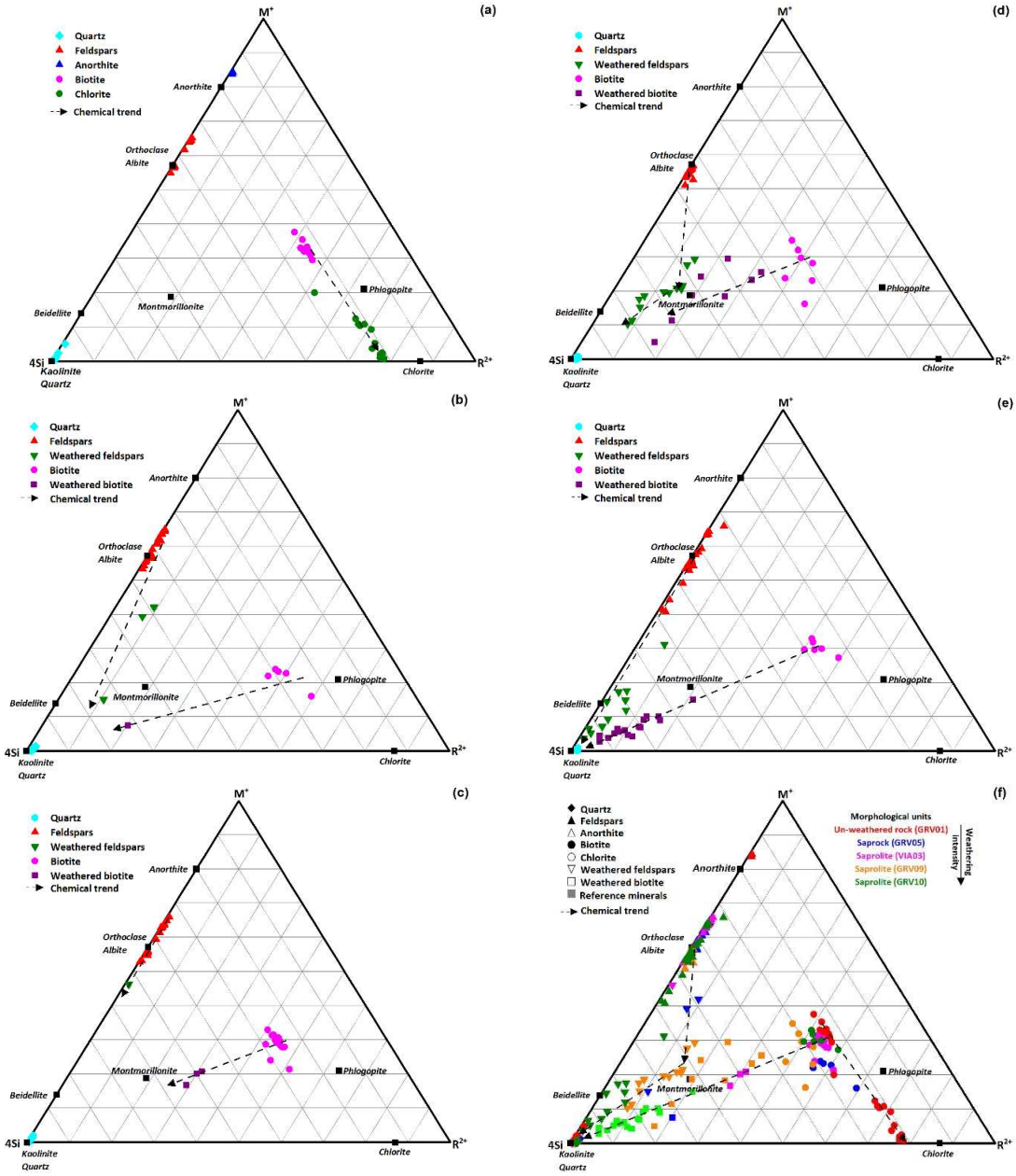

Figure 10: Chemiographic projections of the chemical compositions of the minerals obtained with the SEM EDS probe in the 4Si – M^+ – R^{2+} ternary diagram. (a): un-weathered rock. (b): saprock. Feldspars are weathered into smectite at this stage, biotite is also weathered in smectite but richer in Mg^{2+}. (c) bottom saprolite. Weathered biotites plots between biotite and smectite indicating intermediate composition attributed to mixed layers. (d): saprolite. Weathered feldspars plot towards kaolinite indicating mixture between kaolinite and smectites. Biotite is weathered into smectites. (e): top saprolite. Weathered feldspars and biotites plot towards kaolinite indicating formation of kaolinite in a second step. (f): all samples. Three trend lines are shown. Chloritization of biotite due to post-magmatic alteration. Weathering of biotite into smectite in a first step and in kaolinite into a second step. Felspars are weathered into smectite and then into kaolinite. The trend lines for feldspars and biotites are distinct due to different chemical compositions of the secondary minerals, magnesian for biotite weathering and aluminous for weathering of feldspars.

Table 1: Bulk chemical composition in major elements (wt % oxides)

Morphological unit	Rock	Saprock						Saprolite								Soil
Sample	**GRV01**	**GRV02**	**GRV03**	**GRV04**	**VIA05**	**VIA04**	**GRV05**	**GRV06**	**GRV07**	**VIA01**	**VIA03**	**VIA02**	**GRV08**	**GRV09**	**GRV10**	**GRV11**
SiO_2	64.99	67.18	66.96	67.15	68.80	67.67	66.12	64.76	67.81	67.87	66.68	66.97	64.42	66.02	70.38	62.98
Al_2O_3	16.46	14.81	15.73	15.83	14.30	14.94	15.29	16.29	16.13	15.04	15.43	15.75	17.20	15.46	16.07	18.66
Fe_2O_3	3.68	4.59	3.52	3.60	3.89	3.62	4.40	4.08	2.86	3.74	3.98	3.32	4.54	4.20	2.01	4.83
MgO	1.23	1.32	1.08	1.03	1.14	0.97	0.99	1.15	0.73	0.92	1.12	0.64	1.03	1.04	0.33	0.66
CaO	3.35	3.38	3.21	3.34	3.11	3.00	3.17	2.85	2.64	2.72	3.28	2.97	1.81	0.67	0.73	0.09
CaO*	2.75	2.65	2.64	2.74	2.44	2.36	2.37	2.15	2.17	2.02	2.58	2.34	1.81	0.67	0.73	0.09
Na_2O	3.97	3.79	3.84	4.00	3.69	3.66	3.64	3.73	3.73	4.01	3.98	3.77	2.92	3.74	1.81	0.18
K_2O	3.82	2.71	3.55	3.16	2.58	3.24	2.98	3.93	4.17	2.35	2.66	3.46	3.75	4.51	4.97	2.84
MnO	0.07	0.07	0.06	0.06	0.07	0.06	0.08	0.08	0.05	0.06	0.06	0.05	0.10	0.07	0.03	0.03
P_2O_5	0.18	0.22	0.17	0.18	0.20	0.19	0.24	0.21	0.14	0.21	0.21	0.19	0	0	0	0
TiO_2	0.63	0.68	0.60	0.60	0.67	0.60	0.73	0.64	0.44	0.65	0.69	0.51	0.72	0.72	0.32	0.74
LOI	0.63	0.70	0.75	0.94	1.07	1.82	2.42	1.69	1.76	1.96	1.55	1.81	3.54	3.15	3.07	8.22
Total	99.01	99.44	99.46	99.89	99.51	99.77	100.05	99.41	100.46	99.53	99.64	99.44	100.03	99.57	99.70	99.22

Table 2: Calculation of weathering indices

Morphological unit	Rock	Saprock						Saprolite								Soil
Sample	**GRV01**	**GRV02**	**GRV03**	**GRV04**	**VIA05**	**VIA04**	**GRV05**	**GRV06**	**GRV07**	**VIA01**	**VIA03**	**VIA02**	**GRV08**	**GRV09**	**GRV10**	**GRV11**
CIA (%)	59.65	59.98	59.75	60.13	60.39	60.15	60.99	60.79	60.48	62.36	60.86	60.71	66.99	63.41	68.17	85.73
4Si	270.41	279.52	278.61	279.40	286.26	281.56	275.11	269.45	282.15	282.39	277.44	278.65	268.04	274.70	292.84	262.05
M^+	328.56	300.37	313.61	315.31	284.66	293.79	293.46	305.42	302.99	276.30	301.91	300.90	238.23	240.28	189.80	69.12
R^{2+}	31.60	33.77	27.59	26.31	29.19	24.94	25.75	29.66	18.85	23.72	28.75	16.62	26.94	26.69	8.51	16.65
R^{3+}	368.99	347.83	352.54	355.64	329.14	338.42	355.00	370.68	352.20	341.83	352.48	350.55	394.29	355.77	340.31	426.41
4Si (norm ; %)	42.88	45.55	44.95	44.99	47.70	46.90	46.29	44.57	46.71	48.49	45.62	46.74	50.27	50.71	59.62	75.34
M^+ (norm ; %)	52.10	48.95	50.60	50.77	47.43	48.94	49.38	50.52	50.16	47.44	49.65	50.47	44.68	44.36	38.64	19.87
R^{2+} (norm ; %)	5.01	5.50	4.45	4.24	4.86	4.15	4.33	3.00	3.12	4.07	4.73	2.79	5.05	4.93	1.73	4.79
WIS																
$R^{3+}/(R^{3+}+R^{2+}+M^+)$	0.51	0.51	0.51	0.51	0.51	0.51	0.53	0.53	0.52	0.53	0.52	0.52	0.60	0.57	0.63	0.83
Δ4Si (%)	0	4.67	3.62	3.69	8.44	7.04	5.97	2.96	6.71	9.81	4.80	6.75	12.93	13.71	29.31	56.83

Table 3: Element loss/gains

Morphological unit	Rock	Saprock						Saprolite								Soil
Sample	**GRV01**	**GRV02**	**GRV03**	**GRV04**	**VIA05**	**VIA04**	**GRV05**	**GRV06**	**GRV07**	**VIA01**	**VIA03**	**VIA02**	**GRV08**	**GRV09**	**GRV10**	**GRV11**
τ																
SiO_2	-	-0.04	0.08	0.09	0.00	0.10	-0.12	-0.01	0.49	0.02	-0.06	0.27	-0.13	-0.11	1.15	-0.18
Al_2O_3	-	-0.16	0.00	0.01	-0.18	-0.04	-0.20	-0.02	0.40	-0.11	-0.14	0.17	-0.09	-0.18	0.94	-0.04
Fe_2O_3	-	0.16	0.00	0.03	0.00	0.04	0.03	0.10	0.11	-0.01	-0.01	0.11	0.08	0.00	0.08	0.11
MgO	-	0.00	-0.09	-0.12	-0.13	-0.17	-0.31	-0.07	-0.15	-0.27	-0.17	-0.36	-0.27	-0.27	-0.48	-0.55
CaO	-	-0.06	0.00	0.05	-0.12	-0.05	-0.18	-0.16	0.13	-0.21	-0.10	0.09	-0.53	-0.83	-0.57	-0.98
Na_2O	-	-0.11	0.01	0.06	-0.12	-0.02	-0.21	-0.07	0.34	-0.01	-0.08	0.17	-0.36	-0.18	-0.10	-0.96
K_2O	-	-0.34	-0.03	-0.13	-0.36	-0.10	-0.33	0.02	0.56	-0.40	-0.36	0.11	-0.14	0.03	1.58	-0.37
MnO	-	-0.04	-0.13	-0.12	-0.01	-0.04	-0.03	0.11	-0.07	-0.20	-0.16	-0.05	0.20	-0.10	-0.10	-0.65
P_2O_5	-	0.14	-0.01	0.05	0.05	0.12	0.15	0.16	0.11	0.14	0.07	0.30	-1.00	-1.00	-1.00	-1.00
ε	-		0.08	0.10			-0.05					0.37				

Table 4: particle size distribution of the samples

Morphological unit	Rock	Saprock					Saprolite							Soil
Sample	**GRV01**	**GRV03**	**GRV04**	**VIA05**	**VIA04**	**GRV05**	**GRV06**	**GRV07**	**VIA01**	**VIA03**	**VIA02**	**GRV09**	**GRV10**	**GRV11**
Gravels	94.07	85.49	79.87	80.82	72.70	56.91	46.14	69.10	62.11	68.53	72.90	61.76	45.82	18.38
Sand	2.56	11.11	16.16	15.88	21.88	34.32	46.61	24.55	30.07	23.39	19.69	23.62	32.57	21.04
Silt	1.96	1.73	2.48	2.11	3.61	5.79	5.21	4.48	4.87	5.90	4.86	9.97	15.10	21.47
Clay	1.42	1.68	1.50	1.19	1.81	2.97	2.03	1.87	2.95	2.18	2.56	4.65	6.51	39.11
gravels / (sand + silt)	20.82	6.66	4.29	4.49	2.85	1.42	0.89	2.38	1.78	2.34	2.97	1.84	0.96	0.43

Table 5: Porosity and density measurements obtained by water immersion method

Morphological unit	Sample	Total porosity φ (%)	Bulk density ρb ($g.cm^{-3}$)	Grain density ρg ($g.cm^{-3}$)
Rock	GRV01	1.73±0.01	2.66±0.01	2.71±0.03
Saprock	GRV03	3.57±0.01	2.58±0.02	2.68±0.02
	GRV04	5.47±0.01	2.54±0.02	2.69±0.02
	GRV05	10.54±0.01	2.41±0.02	2.69±0.02
Saprolite	VIA02	11.02±0.01	2.40±0.02	2.70±0.01

Graphical abstract

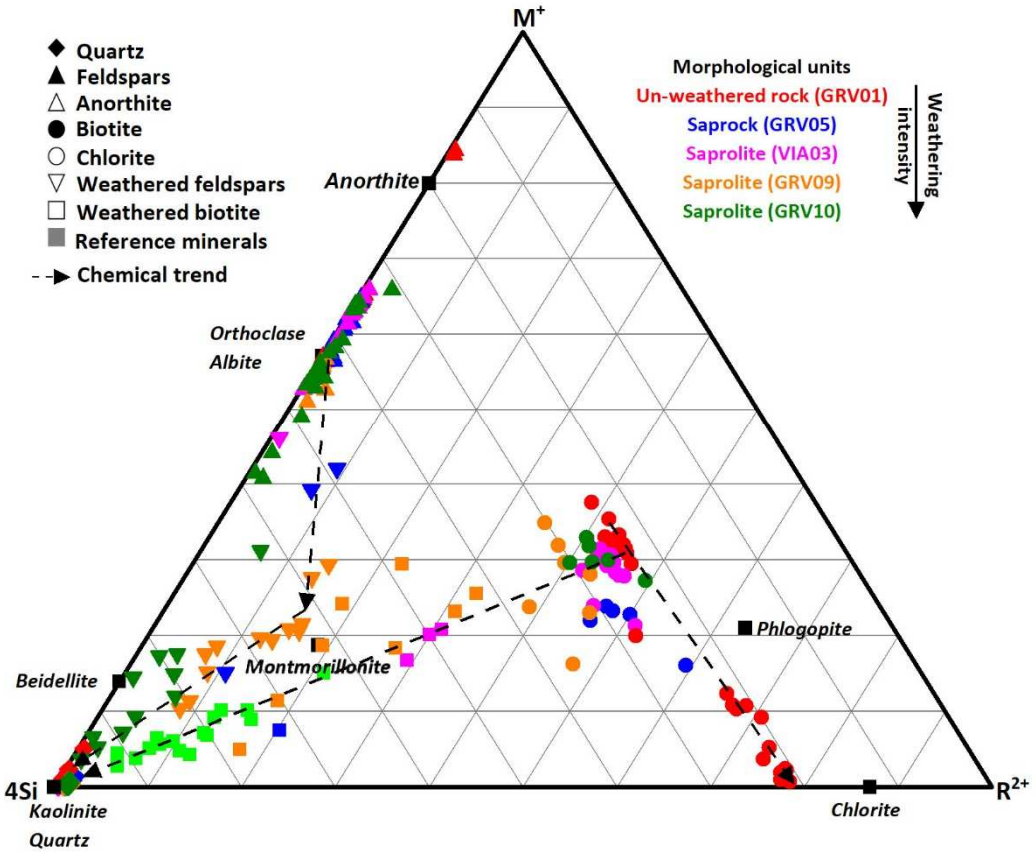

Graphical abstract: Chemiographic projections of the chemical compositions of the minerals obtained with the SEM EDS probe in the 4Si – M^+ – $R2^+$ ternary diagram. The trend lines depict the weathering sequences of the minerals. Chloritization of some biotite of the un-weathered rock due to post-magmatic alteration. Weathering of biotite into smectite in a first step in saprock and into kaolinite in a second step in saprolite. Weathering of feldspars into smectite in saprock and then into kaolinite in saprolite. The trend lines for feldspars and biotites are distinct due to different chemical compositions of the secondary minerals, magnesian for biotite weathering and aluminous for feldspars weathering.